Wind Wave Tank for Experimental Investigation of Momentum and Enthalpy Transfer from the Ocean Surface at High Wind Speed

by

Moshe Alamaro

Mechanical Engineer's Degree (1999)
Massachusetts Institute of Technology

Submitted to the Department of Earth, Atmospheric and Planetary Sciences in partial fulfillment of the requirements for the degree of

[S.M.]
Master of Atmospheric Sciences

at the

Massachusetts Institute of Technology

June 2001

Signature of Author_____

MIT Department of Earth, Atmospheric and Planetary Sciences
May 11, 2001

Certified by_____

Dr. Kerry Emanuel, Professor of Earth, Atmospheric and Planetary Sciences, Thesis Supervisor

Accepted by_____

Dr. Ronald G. Prinn
Head of the Department

Wind Wave Tank for Experimental Investigation of Momentum and Enthalpy Transfer from the Ocean Surface at High Wind Speed

By

Moshe Alamaro

Submitted to the Department of Earth, Atmospheric and Planetary Sciences in partial fulfillment of the requirements for the degree of Master of Atmospheric Sciences at the Massachusetts Institute of Technology

Abstract

Thermodynamic analysis and numerical modeling of hurricane intensity has shown that its is controlled by the enthalpy transfer from the ocean surface and by drag. Direct measurements of drag, evaporation, and sensible heat transfer are not easily performed on the high seas. Therefore, a wind wave tank has been constructed in which a few aspects of a tropical storm are simulated. The air velocity inside the annular tank is comparable to that of hurricane. However, the three dimensionality of the tank obscures the quantitative comparison between experiments and actual conditions over the surface of the ocean at high wind speeds.

The design of the wind wave tank and the initial experiments create a foundation for future and more comprehensive experimental programs. This thesis focuses mainly on the design and engineering of the tank, and on the fluid mechanics of the rotational flow in the tank. It also provides preliminary experimental data on the drag at high wind speeds obtained by using spindown experiments.

Acknowledgement

I would like to thank Peter Morley, Manager of the MIT Machine Shop for building the wind wave tank and for demonstrating exceptional abilities in dealing with unfamiliar problems. Thanks also to Andrew Gallant, Jim Dudley and Scott Spence of the MIT Machine shop.

Thanks also to Wade McGillis of WHOI who provided advice, equipment and funding. Jeff Colton, an undergraduate UROP student exhibited great enthusiasm and his assistance has been instrumental. I would also like to thank the MIT Edgerly Fund for providing the seed funding that enabled this work.

Special thanks to Bob Langer. Professor Langer's interest in solving practical engineering problems and applying science for the benefit of society has been a source of inspiration, making him my role model. I would also like to express gratitude to professor Kerry Emanuel who supervised this work.

1. Description of the wind wave tank apparatus and its features

1.1 Introduction

The wind wave tank has been constructed by Peter Morley at the MIT Machine Shop. The design is based on a wind wave tank that had been built earlier at the Woods Hole Oceanographic Institute by Dr. Wade McGillis (Lundquist, 1999). As shown in Figures 1.1 and 1.2, the tank is made of two, acrylic concentric walls. The water surface is placed, at various heights in the annulus. First Electric Motor Service, Inc., Woburn, MA, has installed the electric motor. The motor's manufacturer is Lincoln Motor, Inc. The electric motor is variable speed and powers the paddle that generates airflow over the water surface. The Paddle has 12 blades that are hinged to a drum. The paddle's drum and blades are made of anodized aluminum to prevent corrosion when the experiments use seawater.

An anemometer measures the wind speed at a height of 42.5 cm above the tank bottom. The anemometer is able to measure air speeds up to these that do not generate spray in the tank. A controller provides an accurate measurement of the motor and paddle RPM. The controller also enables reading of the power input to the electric motor.

At high wind speed, when spray is generated, a direct measurement of air speed is not possible since the anemometer does not function in wet conditions. Therefore, a false bottom has been constructed to replace the water surface at high air speed, see Figure 1.3. This enables the measurement of RPM vs. air speed for a certain elevation of the false bottom. The false bottom is also used to change the height of the water surface for a given amount of rotating water mass. The false bottom is made of four acrylic sections as shown in Figure 1.3. Four poles that pass through the tank bottom support it. The poles can be elevated as needed to place the false bottom at a required height.

1.2 Measuring water velocity

An Acoustic Doppler Velocitimeter (ADV) measures the water velocity in 3 directions. The ADV is inserted into the tank at various heights as required by each experiment. Water velocity is acquired at 1 or 10 Hz. Table 1 provides an example of the data acquired by the ADV.

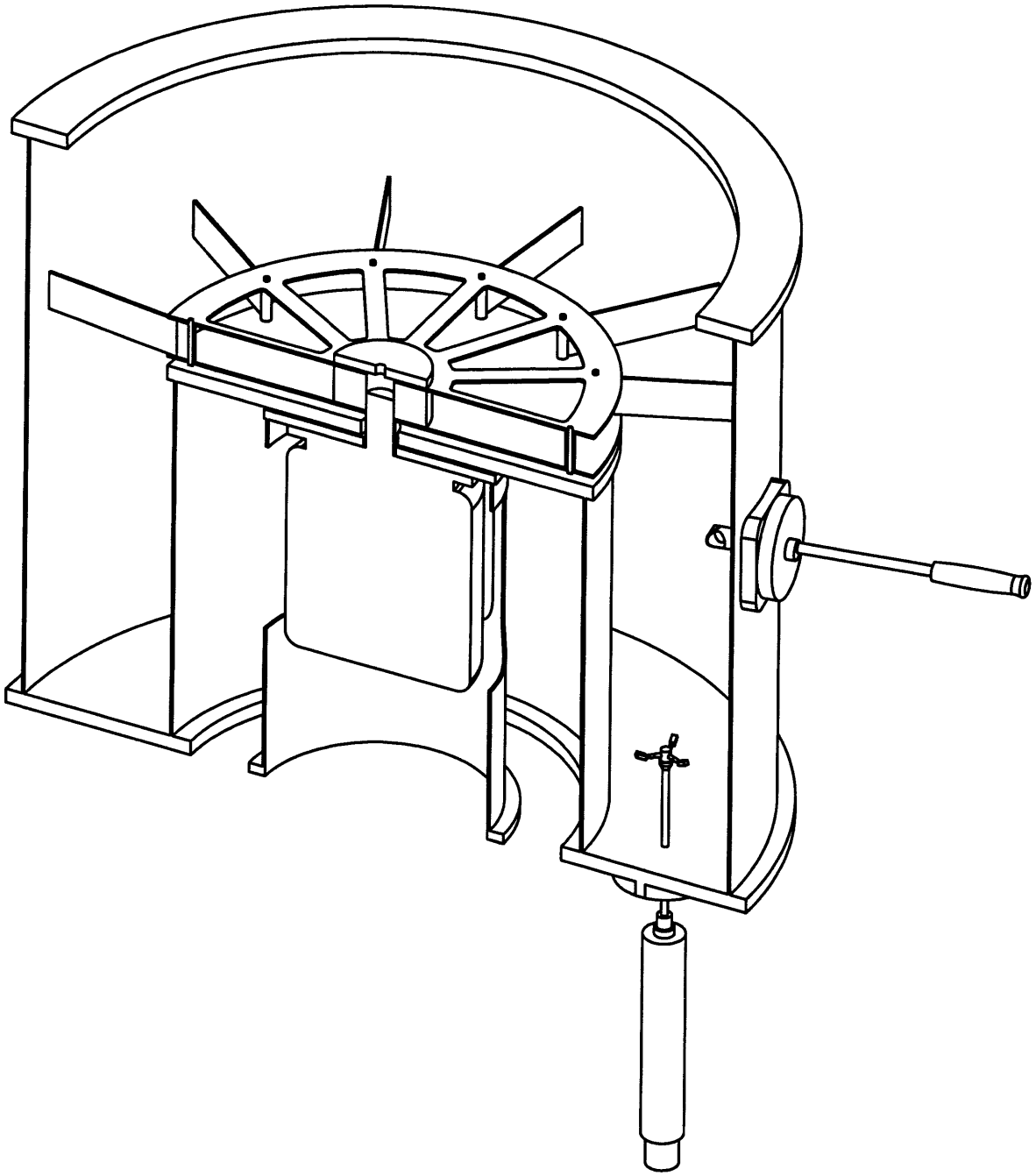

Figures 1.1: Three-dimensional view of the wind wave tank.

Figure 1.2: Cross section of wind wave tank and dimensions.

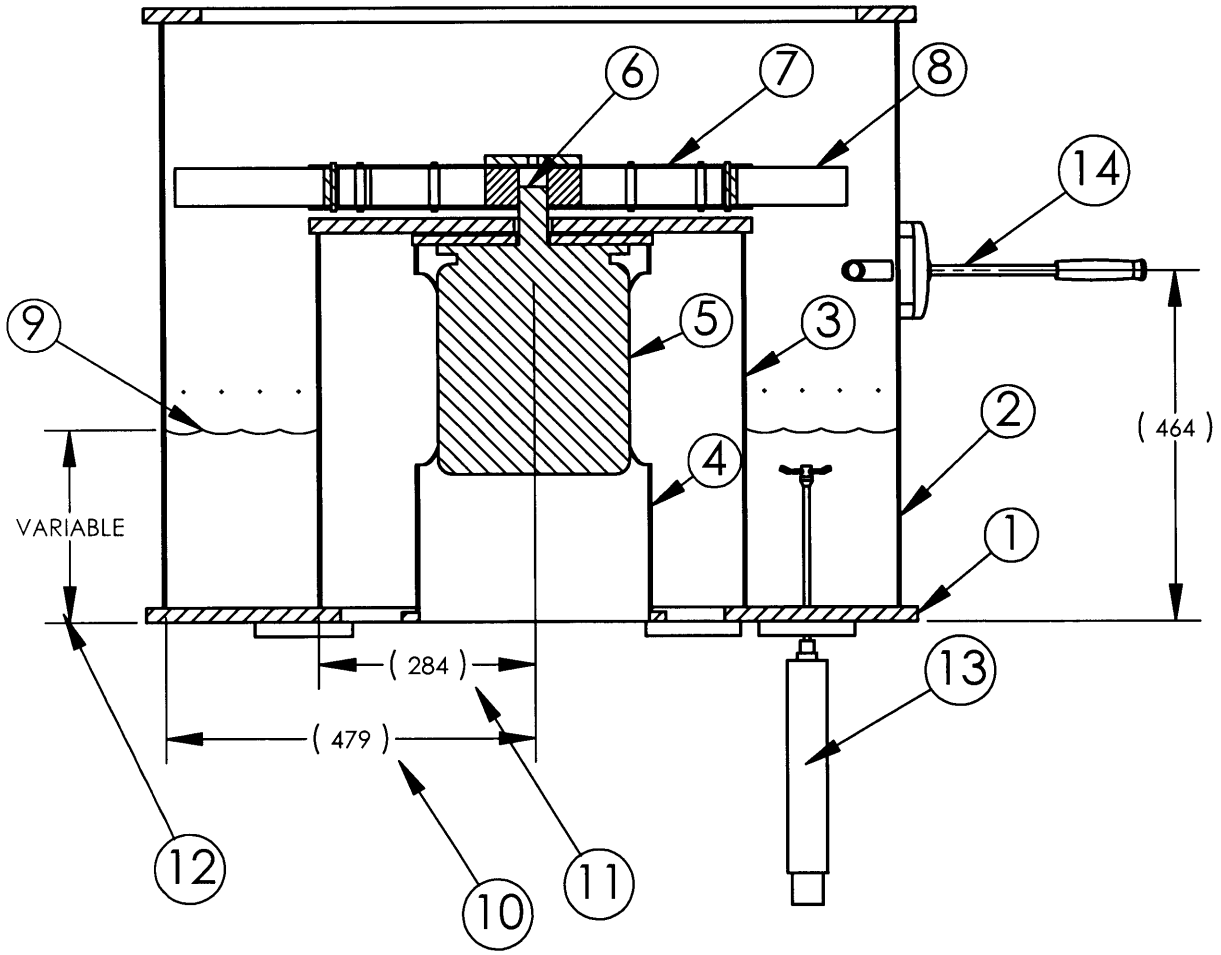

ITEM NO.	DESCRIPTION
1	TANK BOTTOM
2	OUTER TANK WALL
3	INNER TANK WALL
4	MOTOR CASE
5	MOTOR
6	SHAFT
7	BLADE ASSEMBLY
8	BLADE
9	WATER SURFACE
10	RADIUS OF OUTER WALL (479mm)
11	RADIUS OF INNER WALL (284mm)
12	WATER SURFACE (variable)
13	ACOUSTIC DOPPLER VELOCITY METER (ADV)
14	ANEMOMETER
15	ANEMOMETER LEVEL ABOVE TANK BOTTOM (464mm)

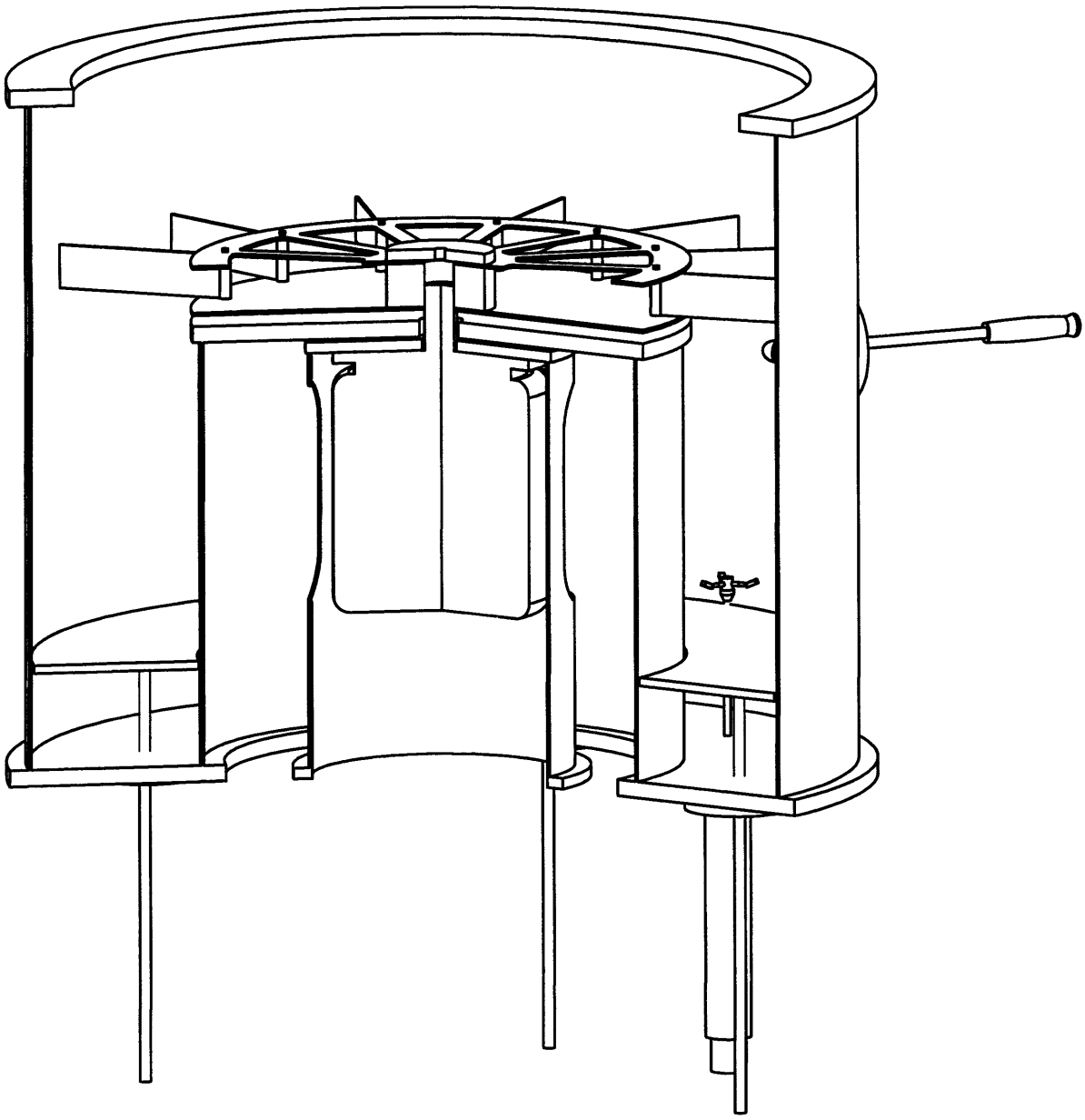

Figure 1.3: False bottom supported by four height-adjustable poles, three of which are shown.

A	V_x	V_y	V_z	S_x	S_y	S_z	C_x	C_y	C_z
-22669	-3547	-664	421	166	162	134	99	96	96
-22668	-3027	-707	50	165	165	133	97	98	96
-22667	-3179	-509	-200	167	166	134	95	98	97
-22666	-3275	-483	138	166	167	135	96	98	96
-22665	-3107	-863	-168	163	165	133	97	98	96
-22664	-3555	-693	-270	165	167	133	96	98	96
-22663	-3769	-448	-8	166	168	135	97	98	97
-22662	-3487	-816	110	166	165	133	97	99	97
-22661	-2882	-986	73	166	169	136	97	98	96
-22660	-2956	-426	-162	167	166	132	95	98	96
-22659	-3381	-422	-443	165	164	133	95	97	96
-22658	-3598	-968	-187	167	167	133	95	96	95
-22657	-3949	-617	-68	171	170	137	97	98	94
-22656	-3723	-975	275	165	165	131	97	98	95
-22655	-2928	-1161	349	168	168	135	98	97	95
-22654	-1704	636	-525	165	165	131	38	38	20
-22653	-3428	-458	-886	169	168	136	95	98	96
-22652	-4227	-1207	-277	168	167	135	91	93	88
-22651	-3504	-1015	283	169	165	136	93	97	97
-22650	-3312	-678	-68	171	170	136	99	98	97

Table 1.1: Sample data provided by the Doppler

In Table 1.1, column A provides the count of each reading, which is spaced by 0.1 or 1 second, depending on the setting of the ADV. The second, third and fourth columns provides the instantaneous water velocity in the x, y and z directions. V_z is the water velocity in the vertical direction, which is not considered in our analysis. The data provided by the last three columns are the correlations between the three components of the water velocity.

The relevant water velocity consists of the horizontal components V_x and V_y. These recorded components of the water velocity depend upon the arbitrary orientation of the Doppler and its three fingers inside the tank. However, our interest is in the tangential horizontal velocity V_θ. Regardless of the ADV orientation, the tangential velocity is given by:

$$V_\theta = \sqrt{V_x^2 + V_y^2} \tag{1.1}$$

The velocity readings in Table 1.1 should be multiplied by 10^{-4} in order have the dimension of the velocity in $m\,s^{-1}$. For example, V_x and V_y of Table 1.1 are used to compute V_θ :

Time	V_x	V_y	$V_\theta(m/\sec)$
0.0	-7931	-475	0.799
0.1	-7216	-979	0.727
0.2	-5880	-912	0.588
0.3	-5011	189	0.512
0.4	-5867	-1067	0.596
0.5	-7330	-1049	0.741
0.6	-6166	-1059	0.620
0.7	-4921	637	0.492
0.8	-5703	48	0.573
0.9	-6364	-604	0.641
1.0	-7345	-726	0.744
1.1	-7411	-1160	0.741

Table 1.2: The three relevant components of the water velocity

1.3 Measuring evaporation

The measurement of water velocity in the tank is required for the estimation of the drag coefficient as outlined in section 3. As for the enthalpy transfer from the tank to the ambient environment, it may consist of both sensible and latent heat transfer.

When evaporation takes place from the water surface, the water temperature is reduced. Our experimental concern is that if the temperature of water is reduced to below the ambient temperature, there should be a heat transfer from the room environment into the water through the tank wall. This heat transfer is difficult to measure. Therefore, in the evaporation experiments, heating elements are placed into the water as shown in Figure 1.4, to keep the water at ambient temperature. Thermocouple measurements of the ambient air and the water temperature are fed into a controller. Based on the temperature difference between the room environment and the water, a transformer provides power to the heating element until the temperatures of the water and the ambient environment are

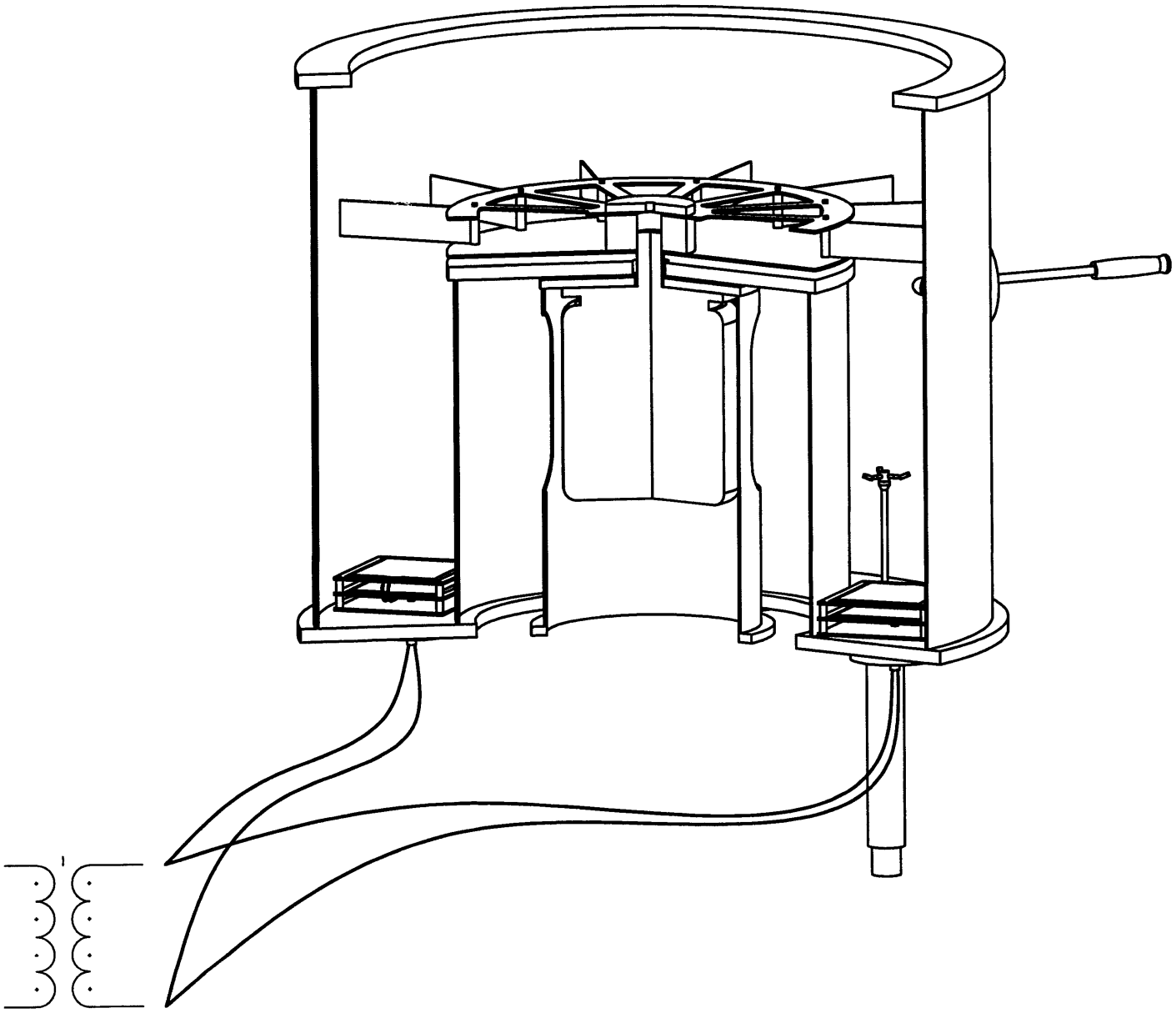

Figure 1.4: Multiple heating elements inside the wind wave tank. A transformer provides power at 24 Volts.

equalized. Since there is no temperature difference between the water and the ambient air, in this experiment the enthalpy transfer consists of latent heat transfer only.

The power and voltage of each heating element is 250 Watt and 24 Volt. The number of heating elements that will be required is not yet determined. It is anticipated that eight to twelve will be used to provide 2 or 3 kW. The low voltage is used for safety reasons. Power is provided to the heating element through holes in the tank bottom.

It is anticipated that the duration of an evaporation experiment will be on the order of hours. During the experiment, a substantial amount of water will evaporate and this will reduce the water level in the tank, increasing the distance from the paddle to the water surface. To prevent this, water will be fed continuously into the tank at the same rate as evaporation. This is performed by a hydraulic system that has been constructed of two external water bottles as shown in Figure 1.5. One external bottle has a valve, the height of which is the same as the water in the wind wave tank. The second external bottle is placed higher than the first one and is connected by a pipe to the valve in the first external bottle. The first external bottle is connected to the water body in the wind wave tank. As soon as water evaporates, the water level in the wind wave tank recedes, causing water to flow from the first external bottle into the wind wave tank. When the water level recedes in that bottle, the valve opens to allow flow of water from the elevated bottle into the first one.

At the end of an evaporation experiment, the total water withdrawn from the elevated bottle is measured. Also, a record of the duration of power supplied to the heating elements will provide information on the total energy provided to the water during the evaporation experiment. This information including the latent heat of evaporation for the water will be used to cross check the accuracy of the computation and interpretation of the evaporation experiment.

1.4 Limitations of the evaporation experiment

The ultimate goal of the wave tank experiments is to simulate the conditions on the high seas. Evaporation from the ocean surface and from ocean spray into the ambient air can be regarded as a two-dimensional. However, during high air speed in the tank, spray is being formed and water film on the tank walls increases the effective evaporation area.

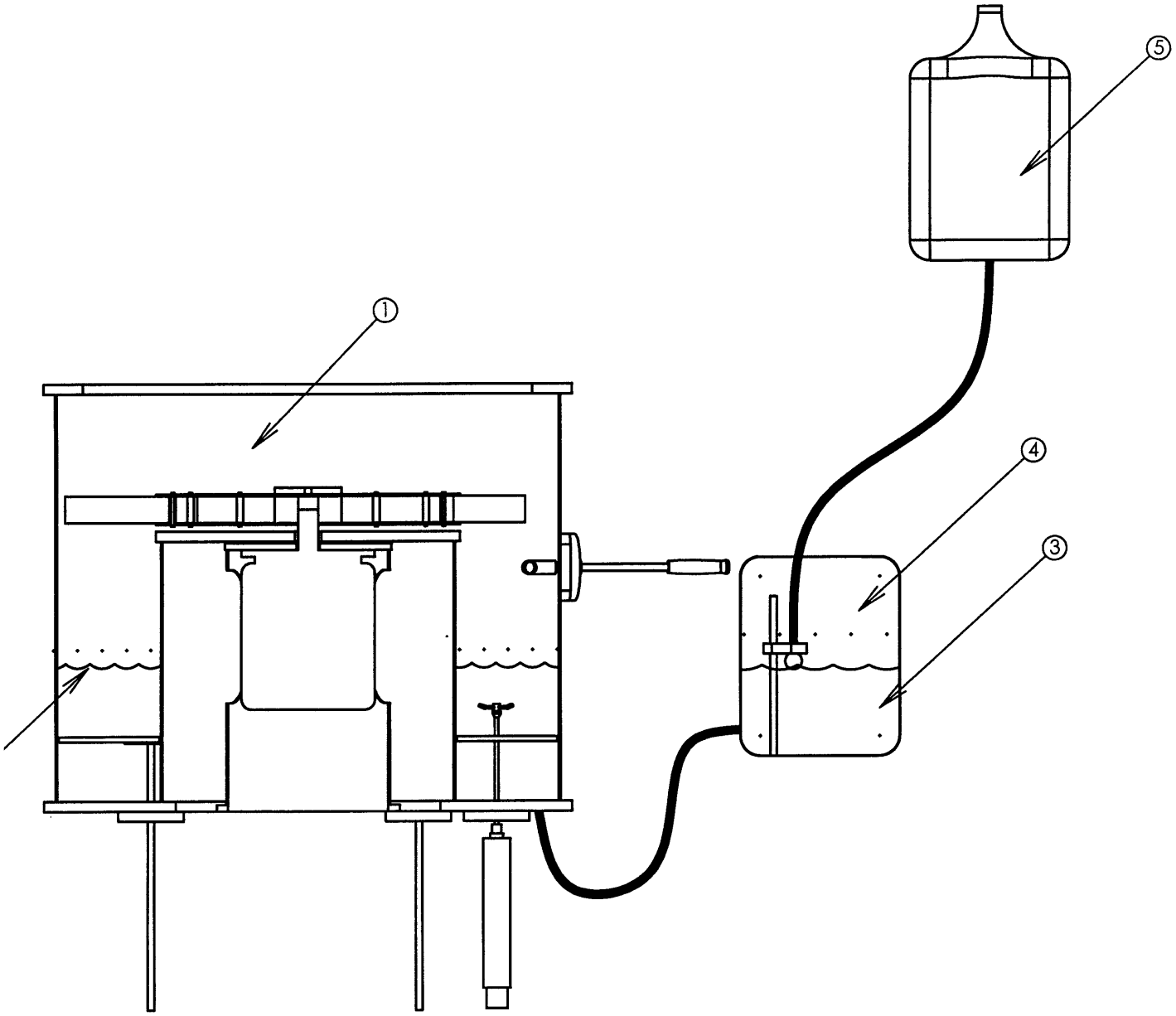

Figure 1.5: hydraulic system that provides water during evaporation.

1) Wind wave tank
2) Water surface in wind wave tank
3) Water surface in the control bottle
4) Water control bottle
5) Elevated reservoir water bottle

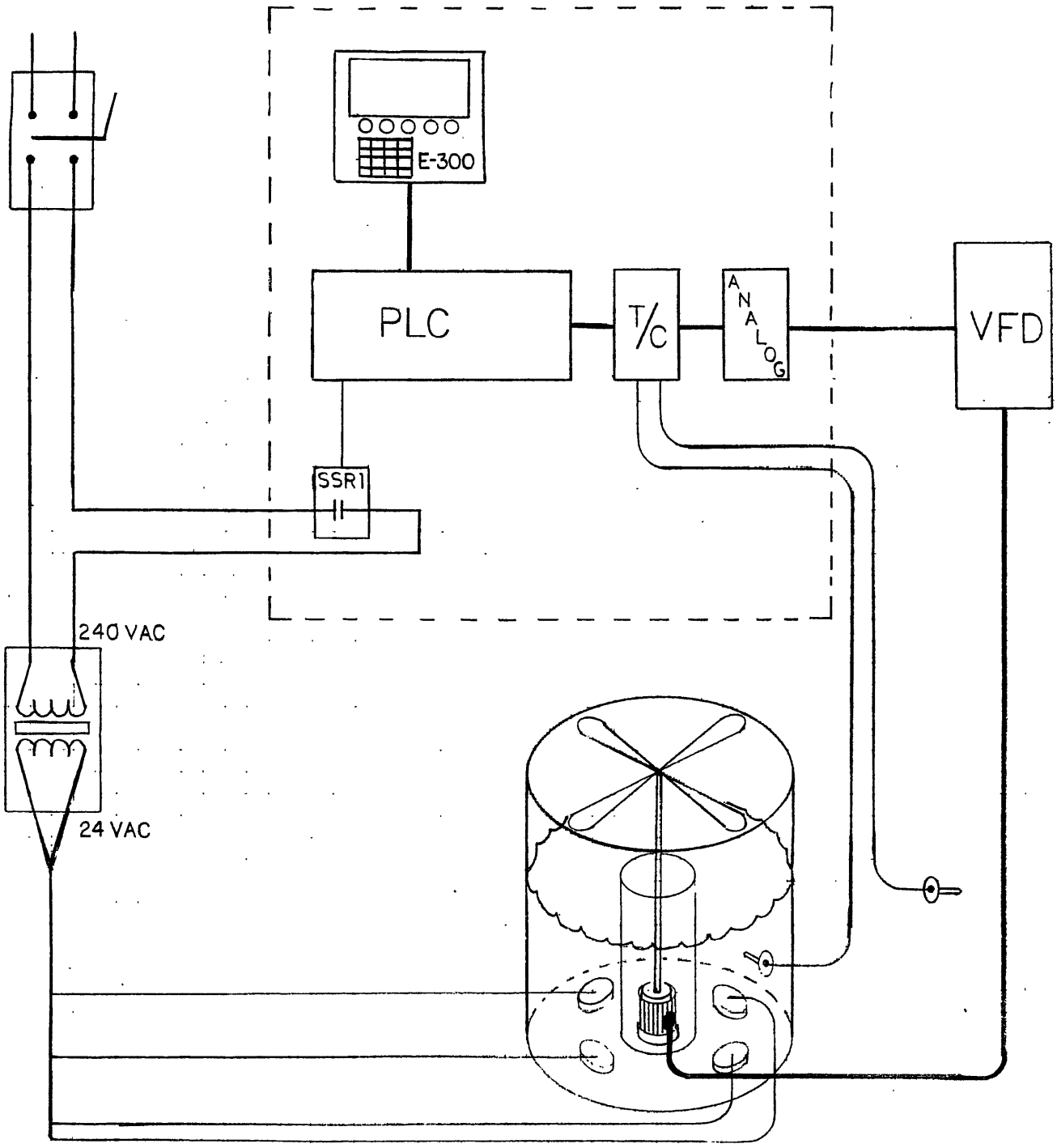

Figure 1.6: Circuit diagram of the evaporation control and water heating system.

a) Thermocouples readings from the ambient air and from the water are fed into the PLC.
b) The PLC does a comparative function and outputs the temperature difference to the SSRI
c) Power output from the VFD is fed into the PLC as an analog input.
d) Power and temperature are displayed on the E-300.

Built by First Electric Motor Service, Inc.

This fact would definitely contaminate the experiments and will make it difficult to compare it with the evaporation from the ocean surface. The discussion in section 4 shows that most of the water spray in the tank forms a film on the outer wall and only small fraction falls back to the water surface.

1.5 The strength of the paddle blades

The aluminum paddle blades are connected to the drum by stainless steel hinges. One concern was that during high RPM, the centrifugal force might cause a blade to detach from its base. Such an event can be catastrophic for the tank. It would also pose a danger to people working near the tank.

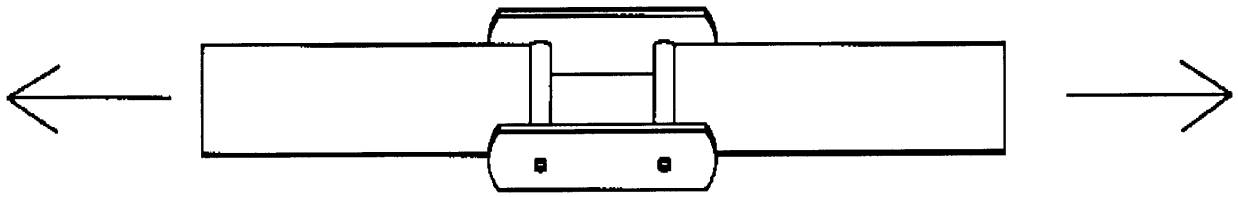

Figure 1.7: Destruction tensile test on the paddle blades

Therefore, a destruction test was conducted at the MIT Impact and Crashworthiness Laboratory, which is directed by Professor Tomasz Wierzbicki. The MIT Machine Shop provided extra blades, which were fastened to a hinge mechanism, similar to the actual one used in the wind wave tank. A tensile force was applied to the two blades until the model was destroyed. A record of the tensile force vs. displacement is provided in Figure 1.7. As shown, at the failure point the load was 13,000 N and the displacement was 5.5 mm. The model failed at the hinge.

The blade weight is 0.1 Kg and its center of gravity is placed 0.4 m from the rotation axis. This information, including the failure load is used to calculate the maximum permitted RPM of the blades.

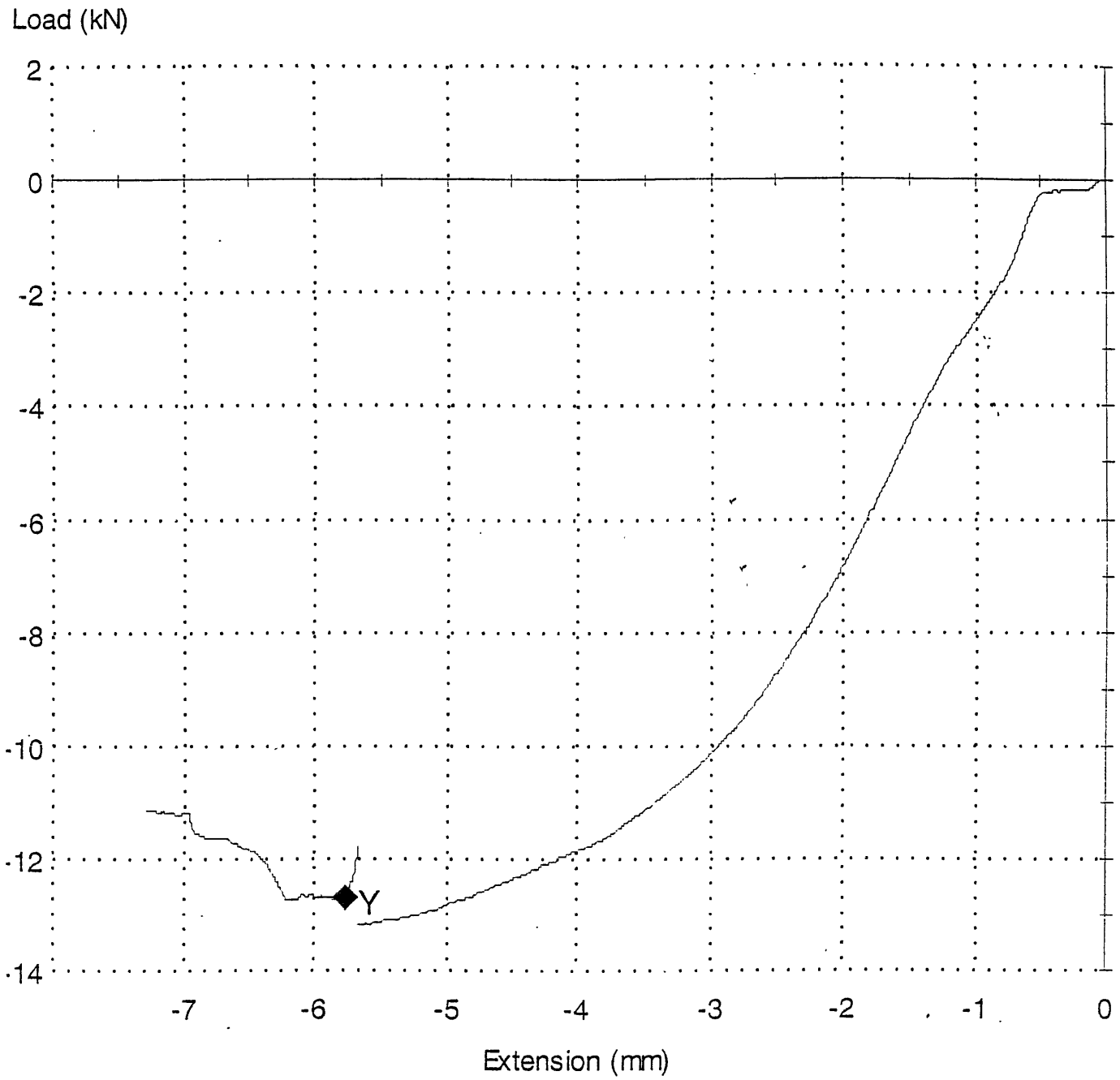

Figure. 1.8: Load vs. extension of the blades destruction test. The test was conducted January 18, 2001. The failure load was 13,000 N.

$$F_{centrifugal} = 13{,}000\ N = m_{bl} \cdot \omega^2 \cdot r = 0.1 \cdot \omega^2 \cdot 0.4 \qquad (1.2)$$

Or
$$\omega = 570 \frac{rad}{\sec} \cong 5{,}400\ RPM \qquad (1.3)$$

Accordingly, a rotation velocity of 5,400 RPM will cause a tensile force that is equal to the failure load of the blade. In our experiments to date the rotation speed never exceeded 1,000 RPM. Since $F_{centrifugal} \propto \omega^2$, it is clear that the centrifugal force on the blades does not exceed 5 percent of the maximum allowed and we have a safety factor of more than 20.

2. Background and objectives of the experimental investigation

2.1 Introduction

Tropical cyclones also known as typhoons in the western North Pacific, and hurricanes in the Atlantic, are a particular phenomenon with frequently disastrous consequences. These are intense cyclones, generated over tropical oceans with a power range of $10^{12} - 10^{13}$ Watt and kinetic energy of 10^{18} Joule or more. As a reference, the power capacity of the world's entire electric grid is on the order of 10^{12} Watt.

The hurricane extends over several hundred kilometers and a calm, central region, "the eye of the storm" characterizes it. In hurricanes, both the energy input and its dissipation mainly occur within a boundary layer between the air and ocean. At high wind speeds of 50-60 $m/\sec$ the boundary layer is essentially filled with ocean spray (Lighthill, 1998). Afterwards, as a hurricane reaches land, disastrous effects of various kinds may occur such as flooding due to intense rainfall, rising sea levels and destruction due to high wind speeds.

Tropical cyclones or hurricanes are enigmas of fluid dynamics. Much remains unknown about the physics of hurricanes; they are difficult to study in situ and it is still impossible to develop laboratory experiments that simulate them exactly. The phenomenon has received comparatively little attention from theoreticians perhaps due to the complex thermodynamics and the inability to develop laboratory analogues. Hurricanes involve complex fluid-dynamic processes, including rotating and stratified flows, boundary layers, sea-air interaction, and multi-phase thermodynamics (Emanuel, 1991).

Most applied research on hurricanes concentrates on forecasting the storm track and the development of warning systems. However, the factors that control the intensity of hurricanes are still poorly understood, resulting in the lack of reliability in forecasting the hurricane intensity (Emanuel, 1991). The evolution of hurricane intensity depends mainly on three factors: the storm's initial intensity, the thermodynamic state of the atmosphere through which it moves, and the heat transfer from the upper layer of the ocean under the core of the hurricane (Lighthill, 1998).

The intensification and maintenance of hurricanes depends on self-induced heat transfer from the ocean, which fuels the storm. The latent and sensible heat transfer is the source of the storm's intensity, resulting in high air speed over the ocean surface. This air motion enhances heat and mass transfer from the ocean, leading to high wind speed and so on. The hurricane's energy depends on strong interaction between the atmosphere and the ocean at extremely high wind speeds. This interaction includes:

(i) Transfer of water vapor from the ocean surface to the atmosphere which is necessary to allow saturation to be reached so that air in the eyewall can rise to great heights; and

(ii) Heat transfer from the ocean to the air; and

(iii) A transfer of momentum from the air to the ocean associated with its frictional resistance and shear stresses.

For a mature "steady-state" hurricane, the available energy input from the ocean surface should equal the drag dissipation over the rough ocean surface (Emanuel, 1988).

2.2 The hurricane as a heat engine

Emanuel (1986, 1988, 1991) pioneered the notion that moist-air thermodynamics allows us to view the hurricane as a heat engine. From this point of view, the entire heat intake occurs over the ocean, and essentially consists of latent heat of evaporation transferred during the long spiral path pursued by winds before reaching saturation. This heat intake occurs at practically constant ocean surface temperature. After that, the heat engine's nearly adiabatic work output phase is concentrated in the eyewall where the moist air ascends. The heat loss phase takes place by radiation to space at stratospheric temperature, which is approximately 200 K.

This heat engine can be modeled as a Carnot engine: one with heat intake and the second with a heat rejection phase. Both phases occur at different constant temperatures and are separated by an adiabatic work output phase. The large difference between the heat intake temperature T_s and the heat rejection phase

temperature T_0 suggests a substantial value for the thermal or "Carnot efficiency" η. The efficiency η multiplied by the heat intake is the mechanical work output. The classical expression for the Carnot efficiency is:

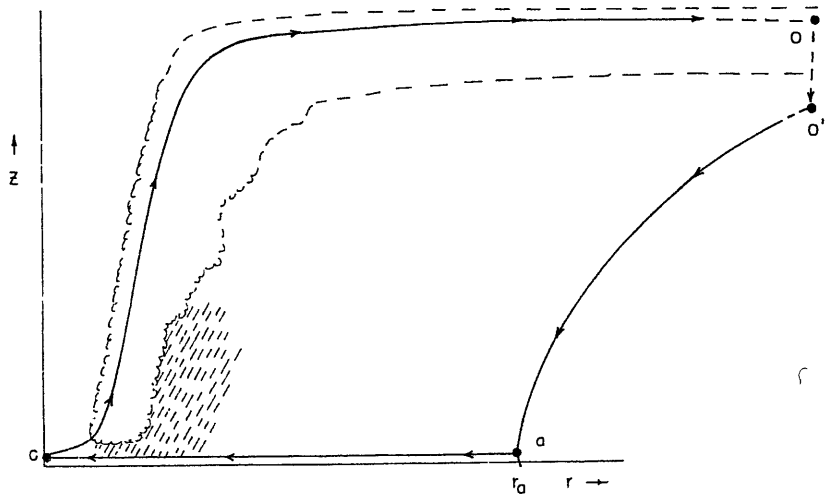

Figure 2.1: The hurricane Carnot cycle. Air begins spiraling in toward the storm center at point a, acquiring entropy from the ocean surface at fixed temperature T_s. It then ascends adiabatically from point c, flowing out near the storm top to some large radius denoted by point o. The excess entropy is lost by radiation to space between o and o' at a lower temperature T_0. The cycle is closed by integrating along an absolute vortex line o' and a (Emanuel, 1991).

$$\eta = \frac{T_s - T_0}{T_s} \tag{2.1}$$

With temperatures in Kelvin. An ideal Carnot engine model for hurricane could take values of 0.33 since a typical sea-surface temperature is 300 K and a typical stratospheric temperature is approximately 200 K.

The mechanical energy output from the engine in the form of extreme winds is required to balance the frictional dissipation of energy occurring near the ocean surface. The study of this balance explains why a hurricane is a tropical phenomenon; the heat intake per unit mass of air depends on the concentration of water vapor under saturated conditions and that concentration according to the Clausius-Clapeyron equation increases steeply with temperature. There is no such dependence on temperature in the dissipation rate per unit mass.

2.3 An engineer's perspective on the hurricane Carnot efficiency

For an engineer who is familiar with or designs real thermal engines, the idea that a natural process such as a hurricane has a practical thermal efficiency, which is equal or close to the ideal Carnot efficiency sounds surprising. The actual efficiency of real thermal systems such as internal combustion engines or thermal power plants is about 0.3 – 0.4. For typical thermal systems, the temperature of the heat intake is about 1,000 K and the temperature of the heat rejection phase is 300 K. Therefore, the ideal efficiency is about 0.67, twice the actual one. On the other hand, a Second Law analysis of natural systems is limited to biological systems in which the temperature difference between the heat reservoirs is limited to a 10-25 K with Second Law efficiencies of about 5-10 percent.

In fact, the analysis below shows that the hurricane thermal cycle efficiency is higher than the classic Carnot efficiency. To show this, let's review first the fundamentals of a classical Carnot engine using the control volume in Figure 2.2 below. Referring to the Carnot reversible engine as a control volume at steady state:

$$\frac{\partial S}{\partial t} = \dot{S}_s - \dot{S}_0 = T_s \dot{Q}_s - T_0 \dot{Q}_0 = 0 \qquad (2.2)$$

Where $\dot{S}_s$ is the flux of entropy from the high temperature reservoir (ocean), $\dot{S}_0$ is the flux of entropy to the low temperature reservoir (space) and $\dot{Q}_s, \dot{Q}_0$ are the heat input and the rejected heat respectively.

The mechanical energy output is computed using the First Law:

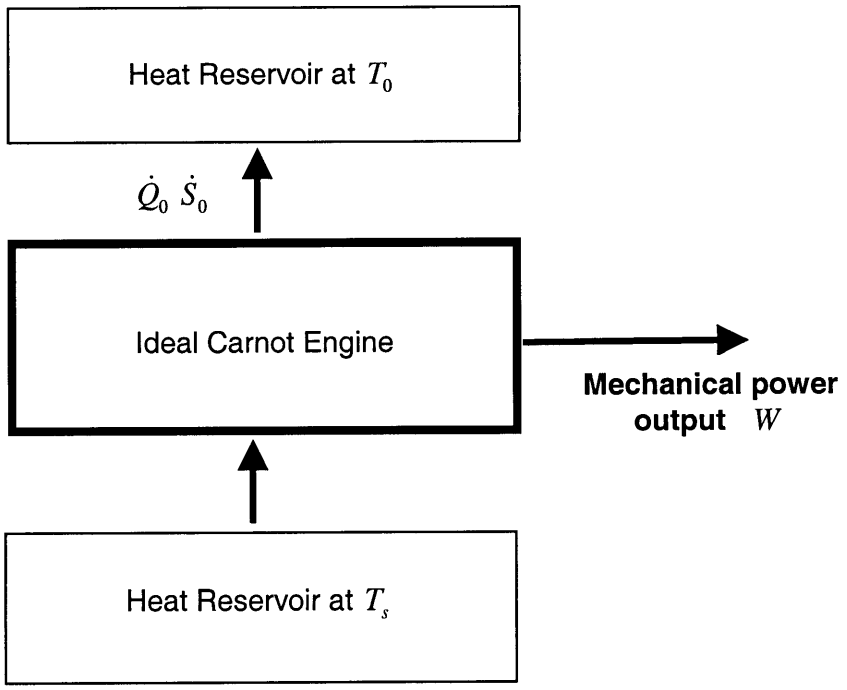

Figure 2.2: Carnot engine model and its heat reservoirs.

$$W = \dot{Q}_s - \dot{Q}_o \tag{2.3}$$

Combining (2.1), (2.2) and (2.3):

$$\eta = \frac{W}{\dot{Q}_s} = \frac{T_s - T_0}{T_s} = 1 - \frac{T_0}{T_s} \tag{2.4}$$

In the model above, the mechanical energy is extracted from the system. However, in the hurricane system, the mechanical power output dissipates over the ocean surface and is converted to heat, becoming a heat input added to $\dot{Q}_s$. Therefore, the heat input into the engine is not $\dot{Q}_s$ but:

$$\dot{Q}_{s_2} = \dot{Q}_s + W = \dot{Q}_s + \eta\dot{Q}_s = \dot{Q}_s(1+\eta) \tag{2.5}$$

The heat input in equation (2.5) is converted to mechanical power by efficiency η. So the mechanical power output at this stage is:

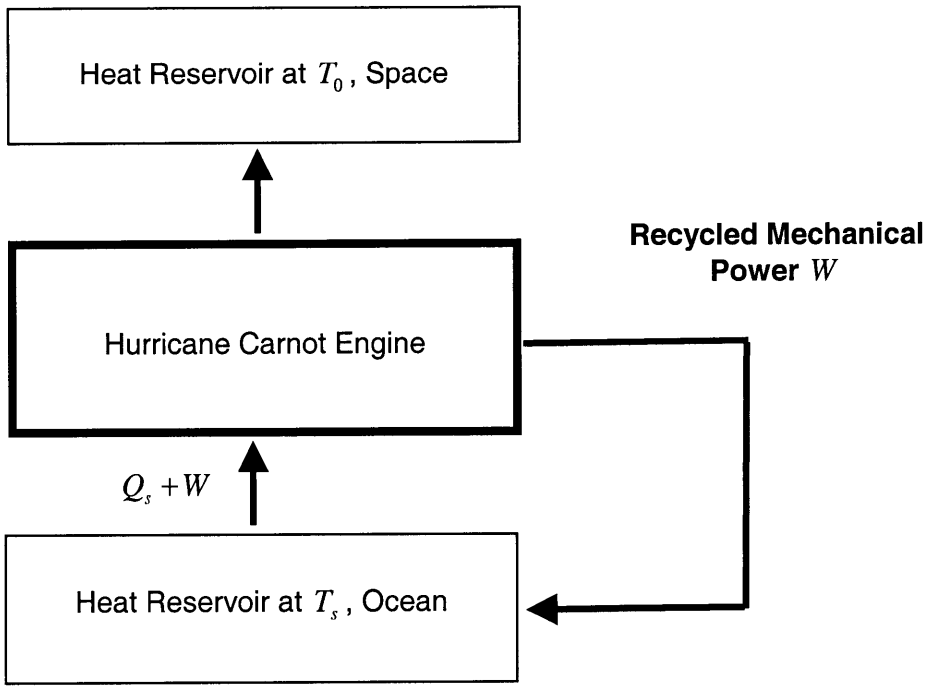

Figure 2.3: Hurricane Carnot engine model and recycling of dissipative energy

$$W_2 = \eta \dot{Q}_{s_2} = \dot{Q}_s (1+\eta)\eta = \dot{Q}_s (\eta + \eta^2) \tag{2.6}$$

Now we can continue with the same reasoning and say that W_2 dissipates over the ocean surface and is converted to heat, becomes a heat input added to $\dot{Q}_s$. The heat input now is:

$$\dot{Q}_{s_3} = \dot{Q}_s + W_2 = \dot{Q}_s + \dot{Q}_s (\eta + \eta^2) = \dot{Q}_s (1 + \eta + \eta^2) \tag{2.7}$$

The heat input in equation (2.7) is converted to mechanical power output by efficiency η. This loop can be performed infinite times, the result of which provides an infinite series:

$$W_{actual} = \dot{Q}_s\left(\eta + \eta^2 + \eta^3 + ...\right) = \dot{Q}_s\left(\frac{\eta}{1-\eta}\right) \tag{2.8}$$

And the actual cycle efficiency of the hurricane Carnot cycle that dissipates and recycles its mechanical output is:

$$\eta_{actual} = \frac{W_{actual}}{\dot{Q}_s} = \frac{\eta}{1-\eta} \tag{2.9}$$

Using the definition for the classic Carnot efficiency η given by equation (2.4) as $\eta = 1 - \frac{T_0}{T_s}$ the expression in (2.9) becomes:

$$\eta_{actual} = \frac{T_s - T_0}{T_0} \tag{2.10}$$

While the classic efficiency is merely:

$$\eta = \frac{T_s - T_0}{T_s} \tag{2.11}$$

The same result can be obtained using alternative reasoning. The mechanical energy output from the hurricane thermal engine is W and the high temperature heat input is $Q_s + W$ as shown in Figure 2.3. Therefore:

$$\eta = 1 - \frac{T_0}{T_s} = \frac{W}{Q_s + W} = \frac{W + Q_s - Q_s}{Q_s + W} = 1 - \frac{Q_s}{Q_s + W} \tag{2.12}$$

Rearranging (2.12):

$$\frac{T_0}{T_s} = \frac{Q_s}{Q_s + W} = \frac{1}{1 + \frac{W}{Q_s}} = \frac{1}{1 + \eta_{actual}} \tag{2.13}$$

Solving (2.13) for η_{actual}:

$$\eta_{actual} = \frac{T_s - T_0}{T_0} \tag{2.14}$$

Which is the same as the result given by (2.10). In fact, this result has been obtained, without using a Second Law analysis by Bister and Emanuel (1998). We explained earlier that for a sea-surface temperature of 300 K and a typical stratospheric temperature of 200 K, the classical Carnot efficiency is 0.33. The revised value is 0.5. As is shown later, this revision provides a 22% higher maximum wind speed.

The last point that may be used to argue that the engine cycle efficiency of hurricanes is even higher than what has been calculated above is the following. Usually, the low temperature heat rejection phase of the Carnot engine is taken as the temperature of the cold reservoir and not the temperature of the heat transmitted to it. That temperature should be the blackbody temperature of space to which the rejected heat is radiated and not the temperature of the stratosphere from which heat is rejected. The blackbody temperature of space is close to absolute zero, and this suggests that the hurricane cycle efficiency is close to unity. This is perhaps a stretch, but using the rejection temperature as the stratospheric temperature of 200 K results, most likely, in a conservative estimate for the value of the actual engine cycle efficiency of hurricanes.

Unlike man-made heat engines, the value for the Carnot efficiency cycle given by equations (2.10) or (2.11) is close to the real value of the hurricane cycle efficiency. The distinction between man made thermal engines and hurricanes is that the mechanical energy produced by real heat engines is virtually extracted out of the system and any irreversibility reduces the cycle efficiency. In hurricanes, irreversibilities in the form of dissipation over the ocean surface lead to a larger heat input into the storm and do not reduce the cycle efficiency. The dissipation is not "useful" work as the work produced by heat engines.

2.4 Energy balance of Hurricanes

The rate of input of available energy into the hurricane from the ocean surface per unit area of the ocean below the storm is:

$$G = \eta C_k \rho_a V_s (k_o^* - k_a) \tag{2.15}$$

Where G stands for "generation", C_k is a dimensionless enthalpy transfer coefficient that accounts for both the latent and sensible heat transfers, V_s is the surface wind speed, k_o^* and k_a are the enthalpies of the ocean surface and the atmosphere near the surface respectively, and η is the cycle efficiency given by equation (2.10) or (2.11).

For a mature hurricane when the storm intensity is steady, the generation given by (2.12) is used up by dissipation over the sea surface. The rate of dissipation per unit area is given by:

$$D = C_D \rho_a V_s^3 \tag{2.16}$$

Where C_D is the drag coefficient. The rate of dissipation is a steep cubic function of the air velocity. Therefore, instead of using the entire area of the ocean affected by the storm, it is accurate enough to consider the area below the eye wall where the surface wind speed is maximum.

Equating the generation and dissipation given by (2.12) and (2.13):

$$V_s^2 = \eta \frac{C_k}{C_D}(k_o^* - k_a) \tag{2.17}$$

We are interested in the maximum of V_s, which is in the vicinity of the eye wall. Therefore, we are also interested in the magnitudes of C_k, C_D and $(k_o^* - k_a)$ in the vicinity of the eye wall where dissipation and enthalpy exchange are maximum. Emanuel (1986, 1988) has shown in a more rigorous analysis that indeed the maximum azimuthal wind speed varies as $\left(\frac{C_k}{C_D}\right)^{\frac{1}{2}}$ where C_k is the exchange coefficient of water and heat (assumed equal) and C_D is the surface drag coefficient.

If the ocean could be considered a flat surface, the similarity between momentum, energy, and water vapor concentration equations could be used to find a simple

relationship between the shear stress (or drag coefficient), the heat transfer and mass transfer. For example, once the shear stress is known for a flat surface, the similarity enables finding the heat transfer coefficient through the use of the Stanton number. Similarly, for a flat surface, once the heat transfer is known, it is possible to calculate the mass transfer coefficient through the use of the Sherwood or Lewis numbers (Incropera, 1996).

However, the ocean surface is not a flat surface and its roughness is a function of wind speed. Andreas and Emanuel (1998) and Lundquist (1999) hypothesized that bubbles and sea spray may be the key to the increase in enthalpy coefficient, decrease of the drag coefficient or both. In high wind conditions, the large flux of momentum into the wave causes wave breaking (visible as whitecapping), which injects air into the water column. At the same time, high winds tear sea-spray droplets directly from the ocean surface, injecting them into the air where they can exchange latent and sensible heat. In hurricanes, these processes are so extensive that the surface of the sea is covered with foam and it is difficult to tell where the ocean surface ends and the air begins. Lighthill (1998) postulated that in hurricane conditions there are three fluids: sea, air and ocean spray. This blurring of the interface could essentially leave the air with nothing to "grab onto" and cause a decrease in the drag. At the same time, the bubbles and sea-spray could greatly affect and increase the latent and heat transfer (Lundquist, 1999).

The exchange coefficients are crucial in the modeling of hurricane growth and maintenance. Rosenthal (1971) found in a series of numerical calculations that while the rate of hurricane intensification is proportional to C_D, the final intensity of hurricane is proportional to $1/C_D$ and the maximum wind speed is proportional to C_k. Emanuel, before discovering the role of dissipative heating determined that the ratio $\frac{C_k}{C_D}$ should be about 1.2 - 1.5 in a severe hurricane, and if the value of this ratio is below 0.75 a hurricane cannot be maintained (Emanuel ,1995). Emanuel's values for $\frac{C_k}{C_D}$ are in sharp contrast with Liu et al (1979) calculations, which found the ratio in high wind speeds to be much less than 1. If Emanuel's model is correct, there should be other still unknown processes that affect these coefficients in high wind speed conditions.

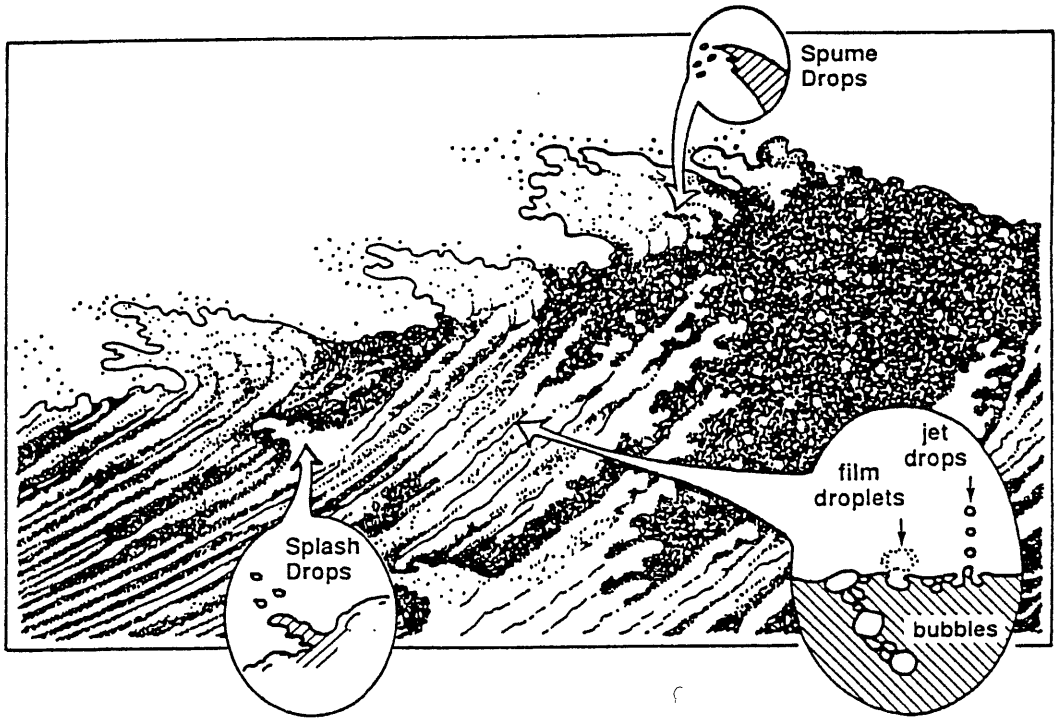

Figure 2.4: Origins of the various kinds of sea spray droplets. Splash droplets arise where wave crests spill at the site of whitecaps. Most film and jet droplets are produced where bubbles rise and burst. Spume droplets are torn directly from the crests of steep waves (Andreas, 1995).

2.5 Current and previous work with circular wind wave tanks

Because it is impractical to take a research vessel into a hurricane, the circular wave tank experiments are intended to provide useful information on the drag and enthalpy coefficients in high air speed over water.

Two notable investigations using circular wind wave tanks have been performed previously (Jahne 1979, Lundquist, 1999). In the first one, the tank total diameter was 75 cm and contained annular water channel of 10 cm depth, 10 cm width and 40 cm inner diameter. In these experiments, gas transfer and friction velocity first grow linearly with wind speed and at a critical speed, the onset of rough waves increases abruptly. The experiment demonstrated the enhancement of air-water exchange by waves. The experiments have also shown that gas exchange is not a function of wind speed alone, nor of friction velocity but also relies on additional parameters such as wave spectra.

The experimental conditions were varied by adjusting the ratio of nitrogen/carbon dioxide, the water velocity and introducing barriers to the flow that increase turbulence (Jahne, 1979).

The second relevant work was performed at Woods Hole Oceanographic Institute by Jessica Lundquist (1999), Wade McGillis and Jim Edson. A circular wind wave tank was used and bubbles were introduced artificially at low air speed. At higher air speed there was no need to introduce bubbles since they were generated naturally by the breaking waves. In these experiments, the drag coefficient leveled when spray was generated.

In both the investigations done by Lundquist and Jahne, spindown experiments were done to obtain the shear stress between the air and the water surface. Similar but more advanced spindown experiments and calculations are outlined in sections 3 and 4 of this work. Both previous investigations assumed that the drag or the skin friction coefficients of the water and the tank walls is not a function of the water speed. This assumption might be wrong since the skin friction is a function of the Reynolds Number of the water flow in the tank. Also, the water motion in the circular tank in the previous investigations was considered to be linear when solving the linear motion equation for the water. This assumption is correct when the width of the annulus is small relative to the radius of the tank.

In this investigation, the water motion is assumed to be in a rigid body rotation. Rotational equations of motion were applied using external torques created by the propelling air motion and the retarding stresses induced by the tank walls. This analysis also assumed variable drag coefficient between the water and walls, which is dependent on the Reynolds Number of the water flow as outlined in section 3.

2.6 The possible role of ocean spray

Over the ocean surface, ocean spray is formed by various mechanisms that are described in section 2.4 (Andreas, 1995). During a hurricane, ocean spray formation gets intensified. The ocean surface temperature during hurricanes is about 27 C whereas the air temperature and humidity are about 22 C and 75% respectively. The hurricane system is comprised of three fluids: ocean, air and ocean spray (Lighthill,

1998). Ocean spray may play an important role in the enthalpy and momentum transfers and that, in turn, determine the hurricane's intensity.

The water drops that constitute the ocean spray are ejected from the ocean surface into the air. The saline water drop temperature is reduced by evaporation cooling to the wet-bulb temperature of the air-saline water system. The minimum temperature is achieved after only about 1% of the water mass is evaporated. The wet-bulb temperature is lower by a few degrees than the air temperature, depending on the relative humidity. Afterwards, depending on the drop size, there are two possible scenarios for the fate of the drop (Emanuel & Andreas, 2000).

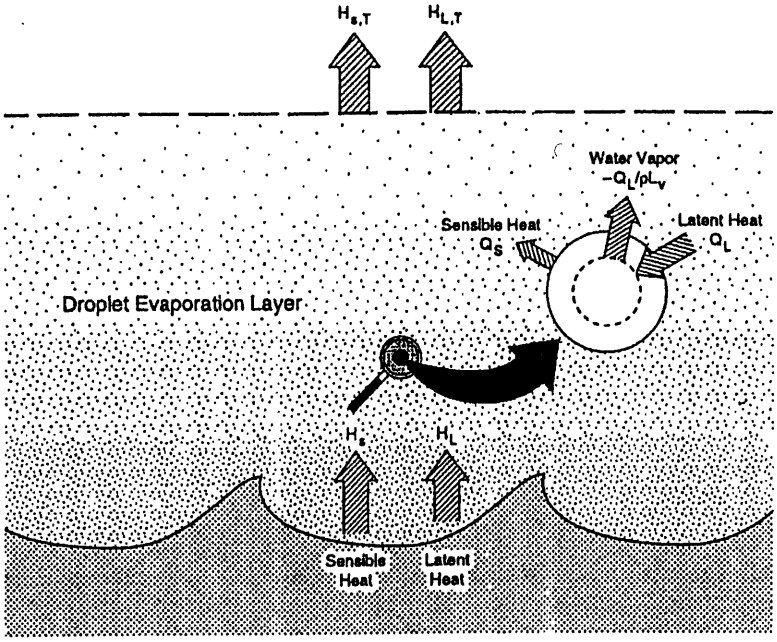

Figure 2.5: Conceptual picture of processes in the droplet evaporation layer (DEL). The ocean exchanges sensible and latent heat through turbulent processes at its interface. The spray drops also exchange sensible and latent heat. The fluxes at the top of the DEL result from these processes, (Andreas, 1999B).

In the first scenario, the drops that are now at about 19 C fall back into the ocean, slightly reducing the ocean surface temperature. This causes heat transfer upward in the ocean thermocline, maintaining the ocean surface at almost constant temperature. New drops are again ejected to form spray and so on. Overall this results in enthalpy

transfer from the ocean to the atmosphere in the form of latent and sensible heat. Here, the air gains both latent heat from the drop mass fraction that evaporates and sensible heat due to the temperature difference between the ocean and the air.

In the second scenario, the water drops are smaller than in the first scenario. Smaller drops have much less inertia relative to their aerodynamic drag (Alamaro, 1999). Therefore, the terminal velocity of such drops is very small so they continue to remain in the air after reaching wet-bulb thermal equilibrium. The flight time is increased and evaporation from the drops continues. In this case, the ambient air, which is warmer than the drops, provides the heat necessary for evaporation. The duration of this process is much longer than the time necessary for the drop to reach a thermal equilibrium (Andreas, 1995). As a result of evaporation, the salinity of the water drop increases. If the drop continues flying in the air, it will eventually reach a "size equilibrium" since for higher salinity, the partial pressure of water vapor over the wet-bulb temperature saline water drop reaches the partial pressure of water vapor in the atmosphere, a point where evaporation ceases.

In the second scenario, when the drop mass is reduced substantially due to evaporation before landing back in the ocean, the ambient air provides the heat necessary for evaporation. Overall, the ambient air provides the heat for evaporation and also gains latent heat, resulting in near zero enthalpy transfer from the ocean to the atmosphere.

Lighthill (1998) speculated that the second scenario might work as a negative feedback if climate change increases the ocean temperature, leading to an increase of enthalpy transfer to the atmosphere, resulting in higher wind speed. According to his hypothesis, the increase in wind speed will result in an increased atomization and formation of smaller drops. Higher wind may also increase the flight time of the drops, leading to their size reduction according to the second scenario outlined above.

One speculative hypothesis is that the second scenario can be induced artificially by adding surfactant to the ocean during hurricanes or promoting the growth of marine surfactants for mitigating their intensity. The surfactant may reduce the surface tension of the sea-water, leading to the formation of smaller drops and overall decrease of enthalpy transfer from the ocean to the atmosphere.

This brief introduction to the possible role of ocean spray makes it clear that water drops formation and aerodynamics play an important but still unknown role in the dynamics of hurricanes. Simulating water spray formation in the wind wave tank with and without surfactants and monolayers is a part of this program. However, the dynamics of ocean spray is very different from the dynamics of water spray formation in the wind wave tank. The analysis in section 4 provides an introduction to the aerodynamics of the water spray in the tank and illustrates the limitation of the experimental apparatus.

2.7 The potential for hurricane mitigation

Tropical cyclones rank among the most deadly and costly natural catastrophes affecting mankind today. In 1970, a single storm killed more than 300,000 people in Bangladesh, while more that 10,000 perished in hurricane Mitch a few years ago. The death toll of such storms has been reduced substantially in developed countries, but the economic toll is still enormous. Hurricane Andrew in 1992 incurred more than $27 billion in damage and it has been estimated (Landsea and Pielke, 1998) that a repeat of the 1926 Miami hurricane would cause more than $75 billion damage, compromising the entire US insurance industry.

Virtually all efforts directed at reducing the risk of hurricanes have focused on forecast, warnings and evacuation, and on improved construction for reducing damages. Warning and evacuation have proven highly effective in reducing loss of life in developed countries. However, developing countries lack the resources necessary for warning and evacuation and due to growing population the potential for loss of life is actually increasing.

The large cost of hurricanes, in terms of lives and property, motivates us to consider ways in which the intensity of these storms might be reduced. It has been known for some time that the tropical cyclone possesses an "Achilles Heel": the molecular interface between the ocean and atmosphere through which water must pass in the process of evaporation. The transfer of enthalpy from ocean to atmosphere when seawater evaporates is the energy source for hurricanes. It is well known that any reduction in the rate of evaporation, which does not also reduce the drag coefficient affecting the flow of air over the sea surface, will reduce the maximum wind speeds of the storms. (Indeed,

the rapid reduction of intensity when storms make landfall is a direct result of the reduction of evaporation from the surface). Moreover, the evaporation need only be reduced over a small region under the storm's eyewall; i.e., over a roughly circular patch of about 150 km diameter. For these reasons, practical techniques could be developed to reduce the enthalpy transfer from ocean to atmosphere needed to sustain hurricanes.

This wind wave tank facility will be used to research and develop hurricane mitigation techniques based on the application of molecular monolayers to the sea surface, known to reduce evaporation in benign wind speed conditions (Barnes and La Mer, 1962). Because the physics of air-sea transfer at very high wind speeds is poorly understood, and because there are no direct measurements of such transfer in high wind conditions, this facility will use mainly empirical approaches to measure the transfer rates and the effect of monolayer substances upon them. This facility is very likely to lead to advances in understanding air-sea exchange at very high wind speeds, and also to the potential development of improved techniques for reducing evaporation from fresh water reservoirs.

In order to artificially induce such a reduction of evaporation, it is proposed to apply a substance to the sea surface that quickly forms a molecular monolayer. A great advantage of such a layer is that only about 2 kg of such substance is required to cover a square kilometer; this can easily be done using a few tanker aircraft. Some oils are better than others at retaining the integrity of a monolayer film under disturbed conditions such as strong airflow. For example, Dr. G. Barnes of the University of Queensland found (in the early 60's) that a 1:1 mixture of hexadecanol and octadecanol was best in re-forming the monolayer cover quickly when disturbed by wind (Barnes and La Mer, 1962). One effect of the addition of monolayer oil to water is the reduction of surface tension. Therefore, even if one cannot see the oil, its presence can be determined through the use of a tensiometer.

Laboratory experiments have concentrated on the effects of monolayers on the rate of evaporation of still water surface. These experiments have shown that significant evaporation retardation only occurs with monolayer molecules that pack closely together (Barnes, 1993, 1997). Such molecules form clusters or domains on the water surface which are essentially impermeable to water molecules (MacNamee et al., 1998). A

monolayer of simple molecules such as the long-chain alcohols will inevitably be disrupted by strong winds and a turbulent water surface. According to Dr. Barnes (Barnes, 2000) two possible ways of overcoming this problem are:

1. Incorporation of a polymeric surfactant into the monolayer. Mixtures of long chain alcohols with several different polymers have been shown to retard the evaporation of water (Fukuda et al., 1979; Drummond et al., 1993). There have been no studies of the domain structures of such monolayers but it is likely that there will be such a structure and that the domains will be more resistant to disruption than domains without polymer.

2. Increasing the spreading rate of the monolayer material. Long-chain alcohols can be spread by broadcasting flakes of the solid alcohol onto the water surface. However, while the rates of spreading are adequate for quiet water surfaces, they would probably not be fast enough for the spreading and repair of a monolayer in the path of a storm. Various materials could be mixed with a long-chain alcohol to increase the spreading rate (Fukuda et al., 1979), but it is possible that such materials would hinder or even prevent domain formation and could therefore render the film ineffective in reducing evaporation.

While it is known that monolayer films substantially reduce the rate of evaporation of planar water surfaces that are relatively undisturbed, very little is known about how such monolayers would behave under the extremely perturbed conditions encountered in hurricanes. It is possible, for example, that the presence of monolayer films would change the characteristics of sea spray, which is thought to constitute the principal mechanism of air-sea enthalpy exchange at high wind speed (Andreas and Emanuel, 1999). Thus, it is proposed that the wind wave tank is used to take an empirical approach by testing various candidate monolayer films in a laboratory experiments designed to simulate the air-sea interface at high wind speeds. The analysis of the wind wave tank characteristics described in this thesis and the preliminary experimental results will be instrumental in the experiments with and without the use of evaporation suppression techniques.

3. Shear stress over the water surface

3.1 Propelling and retarding stresses

The drag coefficient over the ocean surface is defined as:

$$C_D = \frac{\tau_s}{\rho_a \, V_{10}^2} \tag{3.1}$$

Where τ_s is the shear stress caused by the air motion over the water surface, ρ_a is the air density and V_{10} is the relative air velocity at a reference height usually chosen as 10 meters. The following is a simplified model that enables the simulation, measurement, and calculation of the shear stress τ_s over the tank water surface.

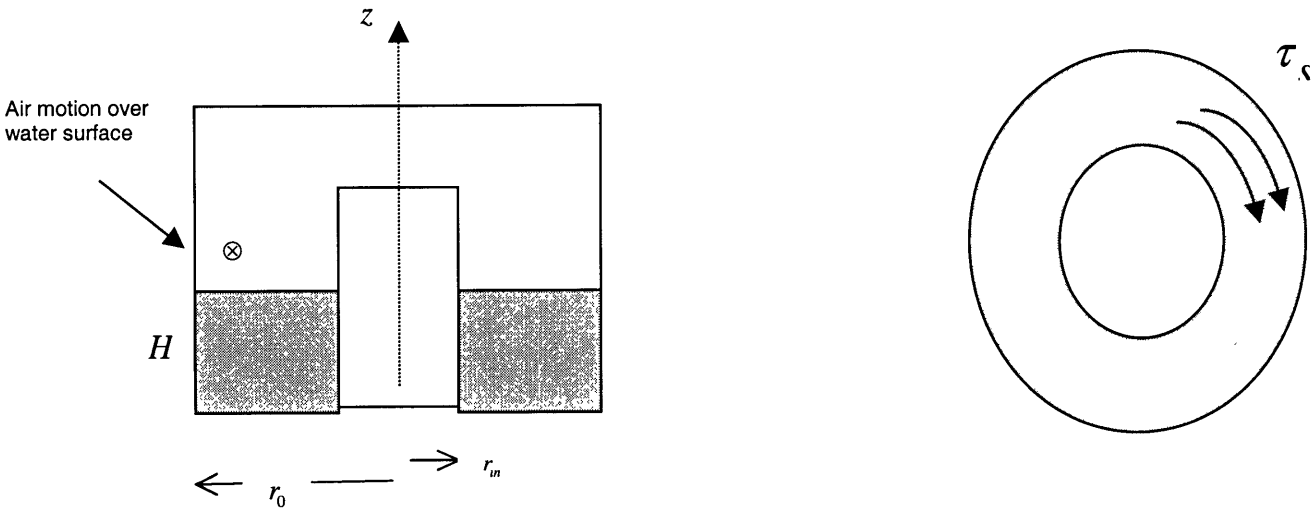

Figure 3.1: Side and upper views of the wind wave tank. Air motion over the water surface results in a propelling shear stress τ_s and propelling torque T_{propel}.

Previous investigations using a wind wave tanks assumed that the water flow in the tank is linear and linear momentum equations were applied (Jahne, 1979, Lundquist, 1999). The linear assumption is valid when the annulus width of the tank is much lower than the tank radius or when:

$$\frac{r_o - r_{in}}{r_{av}} << 1 \tag{3.1}$$

Where:

$$r_{av} = \frac{r_o + r_{in}}{2} \tag{3.2}$$

Using the dimensions of our tank, $r_o = 0.479\,m$, $r_{in} = 0.284\,m$ so $\frac{r_o - r_{in}}{r_{av}} \cong 0.5$.

Clearly, using a linear momentum equation may not be adequate for our investigation. The following treatment uses angular momentum motion equations for the rotating water mass, which is treated as a rigid body.

Assume that the water and air motions in the tank are in rigid body rotation. Assume also that the propelling shear stress is not a function of the radius: $\tau_s \neq \tau_s(r)$. The differential propelling torque provided by the stress applied to a differential water surface area $dA = rd\theta \cdot dr$ is:

$$dT_{propel} = \tau_s dA\, r \tag{3.3}$$

The entire propelling torque is:

$$T_{propel} = \int_{r_{in}}^{r_0} \int_0^{2\pi} \tau_s dA\, r = \int_{r_{in}}^{r_0} \int_0^{2\pi} \tau_s r d\theta \cdot dr\, r = \frac{2}{3}\pi\left(r_0^3 - r_{in}^3\right) \cdot \tau_s \tag{3.4}$$

The outer, inner, and bottom walls provide the retarding torque. The torque due to the outer wall is:

$$dT_0 = \tau_o dA r_0 = -\tau_o r_0 \cdot r_0 d\theta\, dz = -\tau_o r_0^2 \cdot d\theta\, dz$$

Upon integrating:

$$T_0 = -2\pi\, H r_0^2 \tau_0 \tag{3.5}$$

H is the water level and r_0 the outer radius of the tank. Similarly, the retarding torques due to the inner wall and the bottom are:

$$T_{in} = -2\pi\ H\ r_{in}^2\ \tau_{in} \qquad T_{bot} = -\frac{2}{3}\pi\left(r_0^3 - r_{in}^3\right)\cdot\tau_{bot} \tag{3.6}$$

Therefore, the total retarding torque is:

$$T_{retard} = T_0 + T_{in} + T_{bot} \tag{3.7}$$

The total torque on the rigid body rotating water mass is:

$$T_{tot} = T_{propel} + T_{retard} \tag{3.8}$$

3.2 Angular momentum of the water mass and the rotational equation of motion

The differential angular momentum of a differential water mass assuming rigid body rotation with angular velocity Ω is:

$$dM = \rho_w\ \ (r\,d\theta\ dr\ dz)\ (\Omega r)\ r \tag{3.9}$$

And the total angular momentum of the water mass is:

$$M = \rho\,\Omega\int_0^H dz\int_0^{2\pi} d\theta\int_{r_{in}}^{r_0} r^3 dr = \frac{\pi}{2}\,\rho_w\ H\left(r_0^4 - r_{in}^4\right)\Omega \tag{3.10}$$

Equation of motion – the rate of change of the angular momentum is equal to the external total torque:

$$\frac{\partial M}{\partial t} = \frac{\pi}{2}\,\rho_w\ H\left(r_0^4 - r_{in}^4\right)\frac{\partial \Omega}{\partial t} = T_{propel} + T_{retard} \tag{3.11}$$

In steady state: $\dfrac{\partial M}{\partial t} = 0$ or $T_{propel} = -T_{retard}$ (3.12)

3.3 A procedure for measuring and calculating the propelling stress

a. Bring the water to a steady state rigid body rotation under certain V_s - relative air velocity over the moving water surface.

b. Cut the power of the electric motor.

The equation of motion just after the power cut at $t = 0$ when there is no propelling torque is:

$$\frac{\partial M}{\partial t} = \frac{1}{2}\pi\rho_w H\left(r_0^4 - r_{in}^4\right)\frac{\partial \Omega}{\partial t} = -T_{retard} = +T_{propel} \tag{3.13}$$

Measuring $\frac{\partial \Omega}{\partial t}$ just after cutting the power will enable finding the propelling torque and the propelling shear stress. Combining (3.13) with (3.4):

$$T_{propel} = \frac{2}{3}\pi\left(r_0^3 - r_{in}^3\right)\cdot\tau_s = -\frac{1}{2}\pi\rho_w H\left(r_0^4 - r_{in}^4\right)\frac{\partial \Omega}{\partial t} \tag{3.14}$$

The surface shear stress, therefore, is:

$$\tau_s = -\frac{\frac{1}{2}\pi\rho_w H\left(r_0^4 - r_{in}^4\right)\frac{\partial \Omega}{\partial t}}{\frac{2}{3}\pi\left(r_0^3 - r_{in}^3\right)} = -\frac{3}{4}\rho_w H\frac{\left(r_0^4 - r_{in}^4\right)}{\left(r_0^3 - r_{in}^3\right)}\frac{\partial \Omega}{\partial t} \tag{3.15}$$

To obtain $\frac{\partial \Omega}{\partial t}$ of the water mass, the velocity of the water V_w is measured at a distance R_D (the location of the ADV) from the tank center so that: $\frac{\partial \Omega}{\partial t} = \frac{1}{R_D}\frac{\partial V_w}{\partial t}$.

Substituting into (3.15):

$$\tau_s = -\frac{3}{4}\rho_w \frac{H}{R_D}\frac{\left(r_0^4 - r_{in}^4\right)}{\left(r_0^3 - r_{in}^3\right)}\frac{\partial V_w}{\partial t} \tag{3.16}$$

The numeric figures and the tank dimensions used in (3.16) are:

ρ_w - water density $= 1000 \frac{kg}{m^3}$

H - water level in meters, varies from experiment to experiment.

R_D - distance of the ADV from the tank center $= 0.379\ m$

$r_o = 0.479\ m$ outer radius of the tank.

$r_{in} = 0.284\ m$ inner radius of the tank.

Substituting into (3.16):

$$\tau_s = -1{,}050 \cdot H \cdot \frac{\partial V_w}{\partial t} \qquad (3.17)$$

The deceleration of the water mass $\frac{\partial V_w}{\partial t}$ is obtained by spindown experiments that are described in later sections.

3.4 Sources of error - boundary layers

There are inherent fundamental errors in the calculation of the shear stress given by (3.16). The calculation assumes that the water has a uniform angular velocity. In fact, boundary layers in the r direction near the outer and inner walls reduce the moment of inertia of the rotating water in comparison to that of rigid body rotation. Similarly, there are boundary layers in the z direction near the tank bottom and near the water surface as shown in Figure 3.3. Near the corners, there are 3-D boundary layers. A complete analysis of the boundary layers and their effect on the moment of inertia is beyond the scope of this thesis.

The boundary layer near the bottom causes an Ekman flow that together with the surface waves introduce a complexity in the analysis of the experiments as will be shown in later sections.

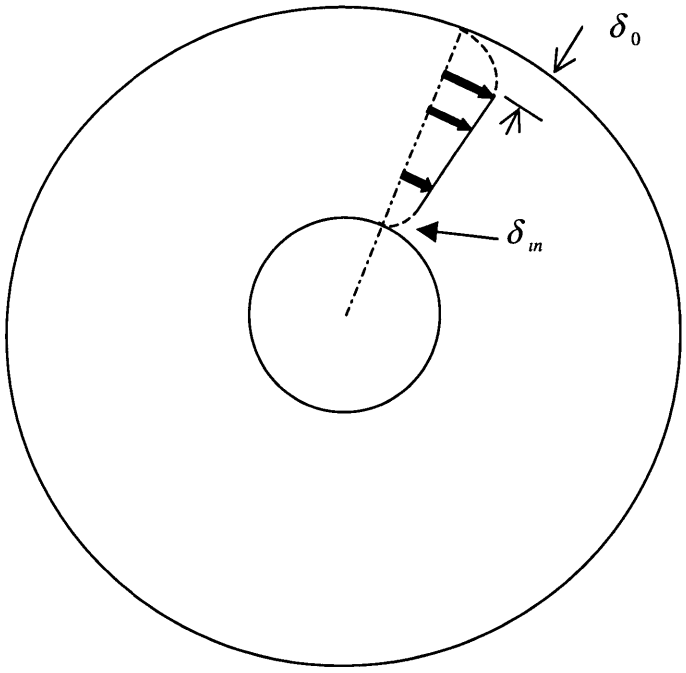

Figure 3.2: Water velocity profile in the radial direction

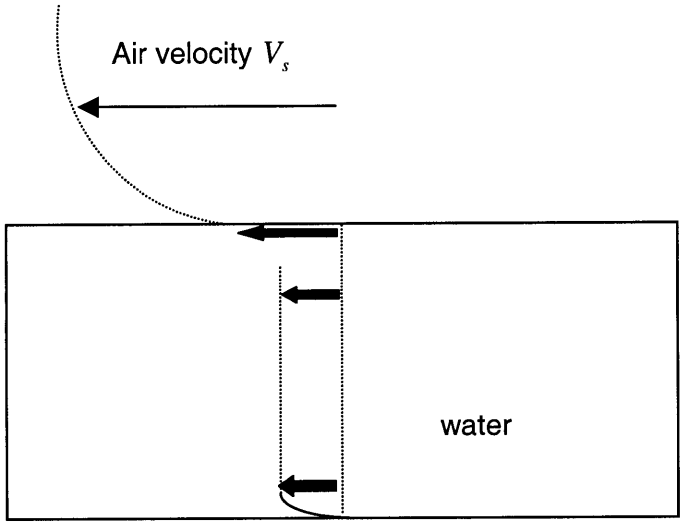

Figure 3.3: Water velocity profile in the z direction

3.5 Parabolic water surface due to rotation

Due to the centrifugal acceleration, the water surface may not be horizontal. The water surface becomes parabolic in r or $H = H(r)$. This changes the elevation of the water. Therefore, defining z_a - the height above the water surface where air velocity is measured is compromised. The water surface area and the water moment of inertia are also changed.

Consider rigid body rotation of the water mass. Equilibrium in the r direction at any point in the water gives:

$$\frac{dp}{dr} = -\rho \frac{V^2}{r} = -\rho\, \Omega^2\, r \quad \text{or} \quad \frac{dp}{dr} = \frac{dp}{dz}\frac{dz}{dr} = -\rho\, g \frac{dz}{dr} = -\rho\, \Omega^2 r \tag{3.18}$$

Integrating:

$$\Delta z(r) = \frac{\Omega^2}{2g}\left(r^2 - r_{in}^2\right) \qquad r \geq r_{in} \tag{3.19}$$

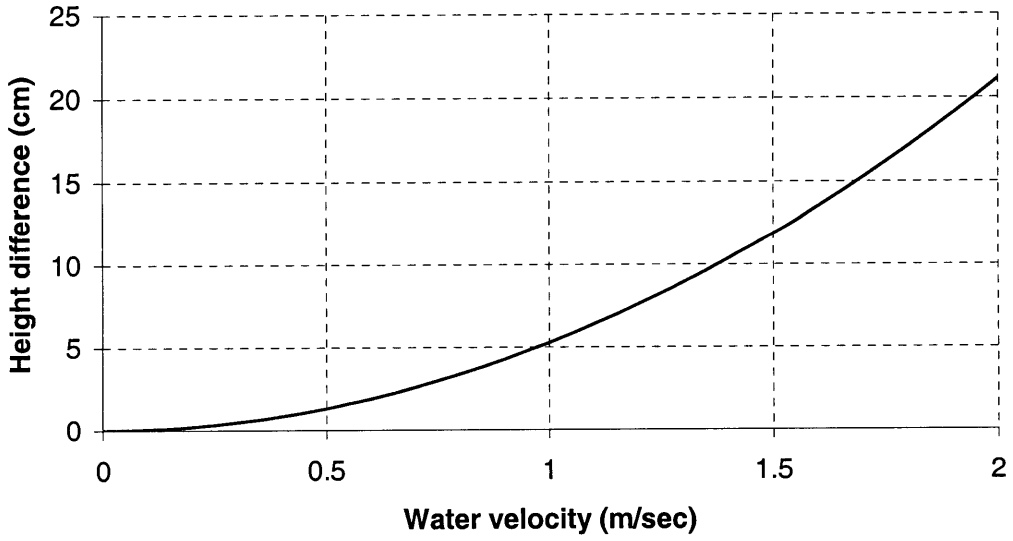

Figure 3.4: Height difference Δz of the water surface between the outer and inner walls as a function of the water velocity at the location of the ADV.

Using $\Omega = \frac{V_w}{R_D}$ and substituting the values for R_D, r_0 and r_{in}, equation (3.19) provides the height difference of the water surface between the outer water and inner walls:

$$\Delta z = 0.0528\, V_w^2 \tag{3.20}$$

In (3.20) Δz is in meter and V_w is in $m/\mathbf{sec}$.

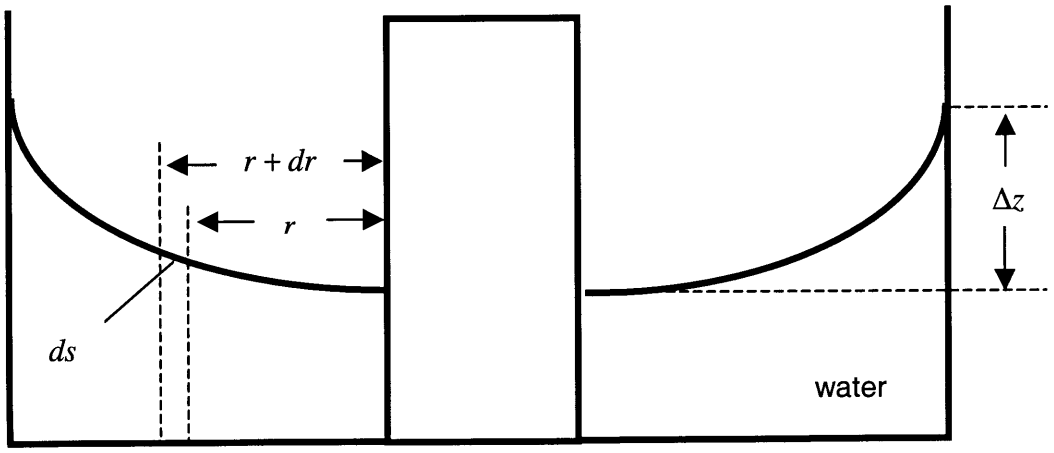

Figure 3.5: Parabolic surface of rotating rigid body water mass

3.6 Parabolic surface area factor

The change in surface area due to rotation is:

$$dA = ds\ 2\pi\ r \quad \text{or} \qquad A(r) = 2\pi \int_{r_{in}}^{r_0} r\ ds \tag{3.21}$$

Where:

$$ds = \sqrt{1 + \left(\frac{dz}{dr}\right)^2}\ dr \qquad \text{and (3.18) gives:} \qquad \frac{dz}{dr} = \frac{\Omega^2}{g} r$$

Substituting:

$$A(r) = 2\pi \int_{r_{in}}^{r} r \sqrt{1+\left(\frac{\Omega^4}{g^2} r^2\right)} \quad dr \tag{3.22}$$

Integrating:

$$A(r) = 2\pi \cdot \frac{g^2}{3\Omega^4} \cdot \left[\left(1+\frac{\Omega^4}{g^2} r^2\right)^{\frac{3}{2}} - \left(1+\frac{\Omega^4}{g^2} r_{in}^2\right)^{\frac{3}{2}} \right] \tag{3.23}$$

The ratio of the new water surface area to the area of the surface without rotation is obtained by substituting in equation (3.23) $r = r_0$: $\Omega = \frac{V_w}{R_D}$.

$$PF_{area} = \frac{2\pi \cdot \frac{g^2}{3\Omega^4} \cdot \left[\left(1+\frac{\Omega^4}{g^2} r_0^2\right)^{\frac{3}{2}} - \left(1+\frac{\Omega^4}{g^2} r_{in}^2\right)^{\frac{3}{2}} \right]}{\pi\left(r_0^2 - r_0^2\right)} \tag{3.24}$$

After substituting the numerical values for R_D, r_0, r_{in} the Parabolic Factor for area becomes:

$$PF_{area} = \frac{2\pi \cdot \frac{9.8^2}{3\left(\frac{V_w}{0.379}\right)^4} \cdot \left[\left(1+\frac{\left(\frac{V_w}{0.379}\right)^4}{9.8^2} 0.479^2\right)^{\frac{3}{2}} - \left(1+\frac{\left(\frac{V_w}{0.379}\right)^4}{9.8^2} 0.284^4\right)^{\frac{3}{2}} \right]}{\pi\left(0.479^2 - 0.284^2\right)} \tag{3.25}$$

Simplifying (3.25) we get:

$$PF_{area} = 8.879 \frac{\cdot \left[\left(1+0.11578\, V_w^4\right)^{\frac{3}{2}} - \left(1+0.0407\, V_w^4\right)^{\frac{3}{2}} \right]}{V_w^4} \tag{3.26}$$

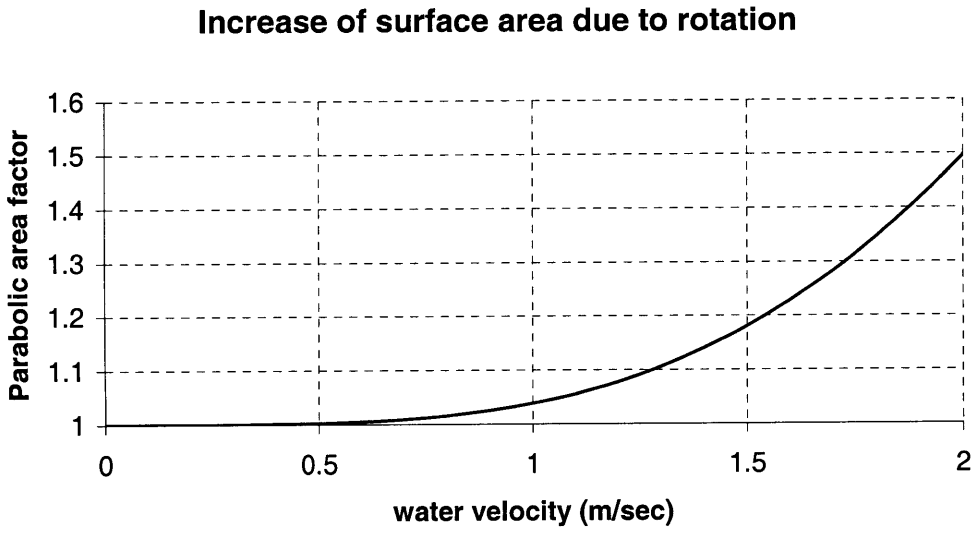

Figure 3.6: The ratio of the surface area due to rotation to the surface area without rotation as a function of the water velocity at the sonic Doppler location.

The increase in surface area due to the rotation of water will be used when evaporation experiments are performed to obtain evaporation rate per unit surface area.

3.7 Parabolic torque factor

The parabolic surface area due to rotation increases the water surface area in comparison to a flat surface. Therefore, there is larger surface area upon which the propelling shear stress may act. The following analysis provides a parabolic torque correction factor for the shear stress that propels the rotational water motion.

The basic assumption is that the shear stress over the water surface is not a function of the distance from the tank center or that $\tau_s \neq \tau_s(r)$. However, since the shear stress now is over a parabolic surface, let's denote the stress as τ_{pf} (where the pf stand for parabolic factor). In Figure 3.7, the stress τ_{pf} acts on a differential surface area $2\pi\, r \cdot ds$ and the differential torque generated by the stress at a radial distance r is:

$$dT_{pf} = \tau_{pf}(2\pi\, rds)r = \tau_{pf}\, 2\pi\, r^2 ds = \tau_{pf}\, 2\pi\, r^2 \sqrt{1+\left(\frac{dz}{dr}\right)^2}\; dr \tag{3.27}$$

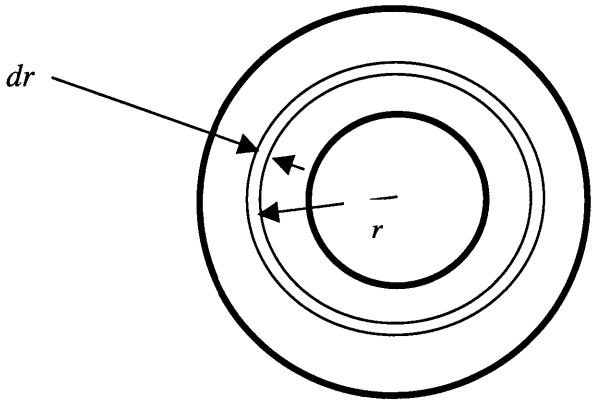

Figure 3.7: Upper view of the parabolic differential water surface area

Substituting $\frac{dz}{dr} = \frac{\Omega^2}{g} r$ and $\Omega = \frac{V_w}{R_D}$ into (3.27):

$$T_{pf} = \tau_{pf}\, 2\pi \int_{r_{in}}^{r_0} r^2 \sqrt{1+\left(\frac{V_w^4}{R_D^4 g^2}\right) r^2}\; dr \tag{3.28}$$

The last expression is the total propelling torque while τ_{pf} is the shear stress over the parabolic water surface. If the water surface were flat, the total propelling torque is given by equation (3.4):

$$T_{propel} = \frac{2}{3}\pi\left(r_0^3 - r_{in}^3\right)\cdot \tau_s \tag{3.4}$$

Using equations (3.28) and (3.4):

$$\tau_{pf} = \left[\frac{\frac{2}{3}\pi\left(r_0^3 - r_{in}^3\right)}{2\pi \int_{r_{in}}^{r_0} r^2 \sqrt{1+\left(\frac{V_w^4}{R_D^4 g^2}\right) r^2}\ dr} \right] \cdot \tau_s = \frac{\tau_s}{PF_{torque}} \tag{3.29}$$

In the last expression the inverse of the term in the bracket provides a correction factor for the shear stress over a parabolic water surface. Substituting the numeric values for r_0, r_{in}, R_D, and g we get:

$$PF_{torque} = 34.48 \int_{0.284}^{0.479} r^2 \sqrt{1+0.504\, V_w^4\, r^2}\ dr \tag{3.30}$$

The last integral has been solved symbolically. The explicit expression for the solution is a long and a cumbersome expression. Therefore, the integral in (3.30) has been solved numerically for $0 < V_w < 2\ m/\mathbf{sec}$. Curve fitting has been performed using Solver of Excel with a sixth degree polynomial to obtain a working formula of the torque parabolic factor as a function of the water velocity. The polynomial expression that was found is:

$$PF_{torque} = 0.0006\, V_w^6 - 0.0209\, V_w^5 + 0.0903\, V_w^4 - 0.0459\, V_w^3 + 0.0184 V_w^2 - 0.0027\, V_w + 1.0001 \tag{3.31}$$

The actual shear stress, therefore, for the rotating water mass in the wind wave tank is obtained by using equations (3.17) and (3.31) is:

$$\tau_{pf} = \frac{-1{,}050 \cdot H \cdot \frac{\partial V_w}{\partial t}}{PF_{torque}} \tag{3.32}$$

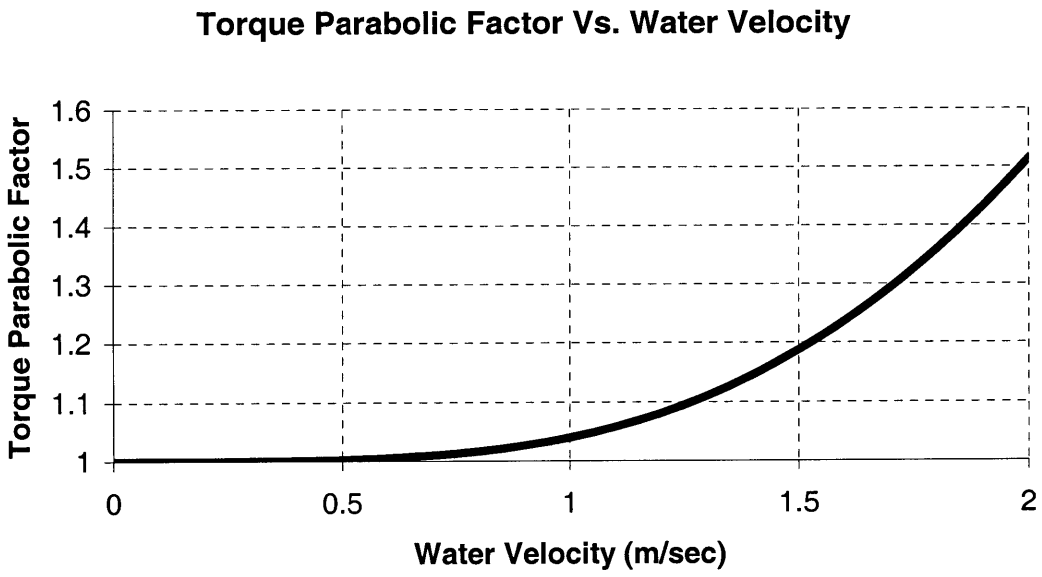

Figure 3.8: The correction factor to the propelling shear stress as a function of water velocity at the radial location of the ADV.

4. Fluid mechanics of rotational water and air in the tank, spindown experiments, and water spray

4.1 Introduction

The spindown technique is at the heart of this investigation. It provides the information on the deceleration of the water mass that, in turn, enables the calculation of the shear stress over the water surface due to the airflow.

The complexity of the experiment is mainly due to the surface waves and inertial oscillations that cause irregular tangential velocity. Ekman flows of both the water and the air also contribute to the flow irregularity. Other factors that contribute to uncertainty are due to instrument noise. It is also possible that the human errors in performing and analyzing the experiments, using unknowingly different standards, have introduced some inconsistencies.

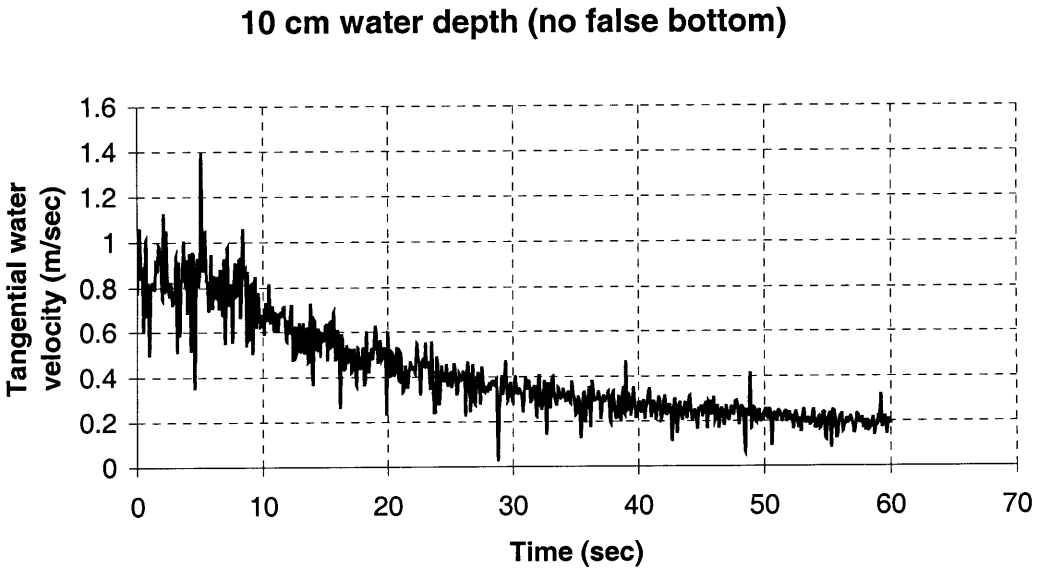

Fig. 4.1: Typical spindown data. Recording rate is 10 Hz. Steady state paddle RPM = 380. The ADV is set at velrange 4. Power is cut off at t = 8 seconds.

4.2 Rotational water motion as a channel flow

We hypothesize that the water flow in the tank can be modeled as a channel flow, if rotational effects are ignored. This flow has a velocity V_w on the order of 0.5 m/sec, and hydraulic diameter D_h on the order of 0.2 m. Therefore, the Reynolds number of the water flow is about:

$$R_e = \frac{V_w D_h}{\nu_w} = \frac{0.5 \cdot 0.2}{10^{-6}} \approx 10^5 \tag{4.1}$$

Therefore, the flow is turbulent.

For turbulent and laminar channel (or pipe) flows, the friction factor f is always a decreasing function of R_e. This is shown graphically by the Moody Chart (Fox, 1998). Semi empirical formulas provide correlations for $f(R_e)$ for various ranges of R_e. For example, the Blasius correlation gives (Fox, 1998):

$$f = 4C_f = \frac{0.316}{R_e^{0.25}} \qquad \text{for } R_e \leq 10^5 \tag{4.2}$$

Here C_f is the C_{DW} that we use for the drag that slows down the water during the spindown experiment due to the retarding shear stress over the tank walls. This is not the drag coefficient between the water surface and the airflow. According to the Moody Chart and the Blasius correlation, for turbulent or laminar flow, C_{DW} is a decreasing function of R_e.

The ODE describing the spindown is:

$$\frac{\partial V_w}{\partial t} = -A\rho_w C_{DW}(R_e) V_w^2 = -k_1 C_{DW}(R_e) V_w^2 \tag{4.3}$$

Where A is the wet wall area, ρ_w is the water density and k_1 is some constant for a specific experiment.

Assume that for a turbulent flow, C_{DW} is a power function of the Reynolds number or equivalently, a power function of the water velocity:

$$C_{DW} \propto R_e^x \propto V_w^{\ x} \tag{4.4}$$

Case 1: $C_{DW} = const$ or $x = 0$. The solution for equation (4.3) for this case is:

$$V_w(t) = \frac{V_m}{(1 + k \cdot t)} \tag{4.5}$$

Here $V_m = V_w(t = 0)$ and k is some constant. This is the solution to the motion equation that was used in previous circular wind wave tank experiments (Lundquist, 1999, Janeh, 1979).

Case 2: $$C_{DW} = C_{DW}(R_e) = C_{DW}(V_w) \propto V_w^{-0.25} \qquad x = 0.25 \tag{4.6}$$

This is the case given by the Blasius correlation described in equation (4.2), see Fox (1998). Substituting into (4.3):

$$\frac{\partial V_w}{\partial t} = -k \ V_w^{7/4} \tag{4.7}$$

Solving the last ODE:

$$V_w(t) = \frac{V_m}{(1 + k \cdot t)^{4/3}} \tag{4.8}$$

Here $V_m = V_w(t = 0)$ and k is some constant.

Case 3: $C_{DW} = C_{DW}(R_e) = C_{DW}(V_w) \propto V_w^x$ while x is any number.

Substituting into (4.2);

$$\frac{\partial V_w}{\partial t} = -k \; V_w^{\,2+x} \tag{4.9}$$

Solving the last ODE:

$$V_w(t) = \frac{V_m}{(1+k\cdot t)^{\frac{1}{1+x}}} = \frac{V_m}{(1+k\cdot t)^n} \tag{4.10}$$

Where $n = \frac{1}{1+x}$, V_m is the water velocity at $t = 0$ and k is some constant. Also:

$$x = \frac{1-n}{n} \tag{4.11}$$

For x to be negative as required by the Blasius correlation or by the Moody Chart, it is required that:

$$n > 1 \tag{4.12}$$

4.3 Data processing for spindown experiments

A complete procedure for the spindown experiment and its analysis is provided in Section 5. The following is an example of a representative spindown experiment and its curve fitting.

Refer to Figure 4.1. The data given in Figure 4.2 is derived from Figure 4.1, which is shifted by 8 seconds, the point at which the spindown starts. The curve fitting is done for the duration of 60 seconds. For this specific case $V_m = 0.84\ m/\sec$

Case 1: $C_{DW} = const$ or $x = 0$. The solution for this case is: $V_w(t) = \frac{V_m}{(1+k\cdot t)}$

The curve fitting has been done using the Solver command in Excel. The best curve fitting for case 1 is: $V_w(t) = \frac{0.84}{(1+0.06927\cdot t)}$ and the least sum of the square of the errors is: $ls = 2.171$

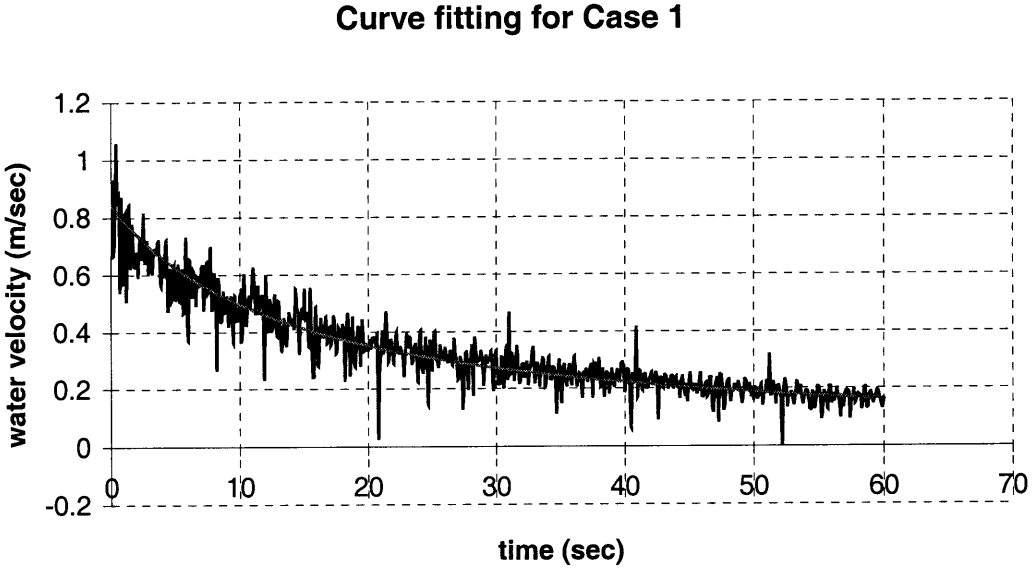

Figure 4.2: Curve fitting for case1. The least square is $ls = 2.171$

Case 2: This case is when $C_{Dw} \propto (R_e)^{-0.25}$. The curve fitting results in

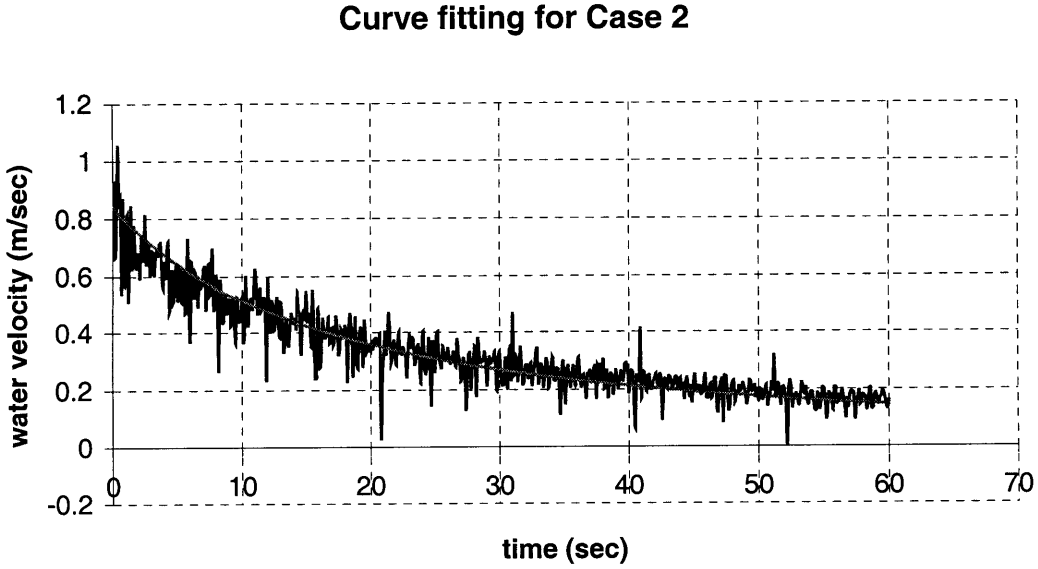

Figure 4.2: Curve fitting for case 2. The least square is $ls = 2.338$

Case 3: In this case no assumptions are made about the dependency of the drag coefficient on the Reynolds number. Iteration is done by Solver on both k and n. The result:

$$V_w(t) = \frac{V_m}{(1+0.0092374 \cdot t)^{0.8407}} \qquad ls = 2.1372$$

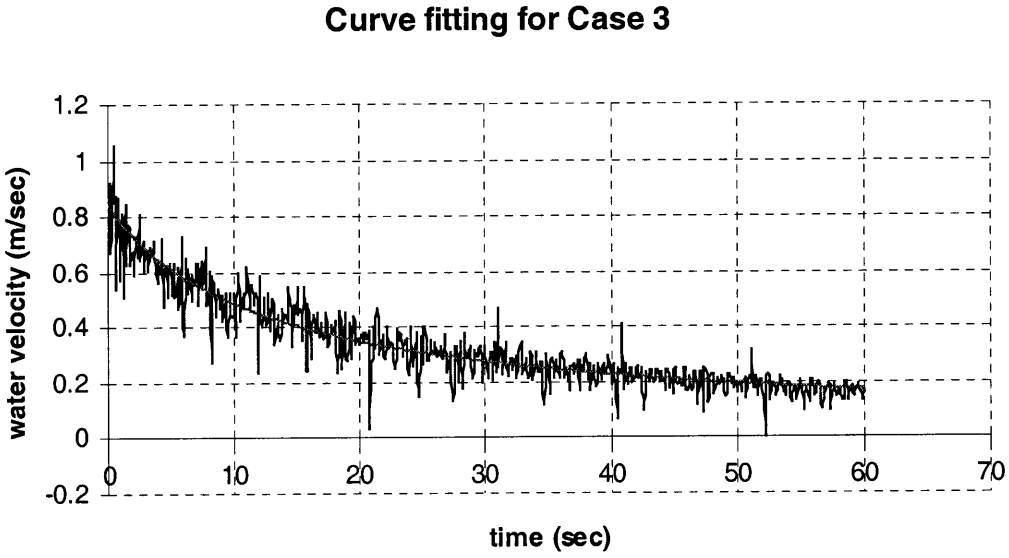

Figure 4.2: Curve fitting for case 3. The least square is $ls = 2.1372$

4.4 Data analysis

Case 3 gives the best curve fit result of:

$$V_w(t) = \frac{V_m}{(1+0.0092374 \cdot t)^{0.8407}}$$

$n = 0.8407$ and using equation (4.11):

$$x = \frac{1-0.8407}{0.8407} = +0.19$$

This implies that: $C_{DW} \propto V_w^{0.19} \propto R_e^{0.19}$ or that the drag coefficient is an increasing function of the Reynolds number, in contradiction to the Moody Chart or the Blasius equation. Such results have been obtained for a portion of the curve fittings while other curve fitting results have shown that $n > 1$ or $x < 0$ for which the drag coefficient is indeed a decreasing function of R_e.

We found that $n > 1$ always if the ADV recording setup is changed. The first step is to change the recording rate from 10 Hz to 1 Hz. The second point is that the ADV should be set to detect water velocity for the following four ranges:

velrange 1 for $\pm 3\ cm/\mathbf{sec}$.

velrange 2 for $\pm 30\ cm/\mathbf{sec}$.

velrange 3 for $\pm 100\ cm/\mathbf{sec}$.

velrange 4 for $\pm 250\ cm/\mathbf{sec}$.

The range of water velocities in the experiments is $1.0 < V_w < 180 \quad cm/\mathbf{sec}$. Our experience has shown that for experiments where the water velocity is greater than $45\ cm/\mathbf{sec}$, the setting that provides the most consistent data and the best correlation is velrange 4. For water velocity less than $45\ cm/\mathbf{sec}$, the best setting is velrange 2.

The problem is that the spindown experiment should be done as shown in section 5 from the highest water velocity, which is about 180 cm/sec to the lowest velocity, which is about 1 cm/sec. Since it is impossible to change the setting of the ADV during the spindown, we decided to perform two spindown experiments instead of one. The first is done by setting the ADV to velrange 4 for a spindown from the highest RPM or the highest water velocity down to 45 cm/sec. The second spindown (for the same experiment) is done from an RPM that corresponds to a water velocity of 45 cm/sec down to about 1 cm/sec. Figures 4.3 and 4.4 shows such spindown data and their curve fits.

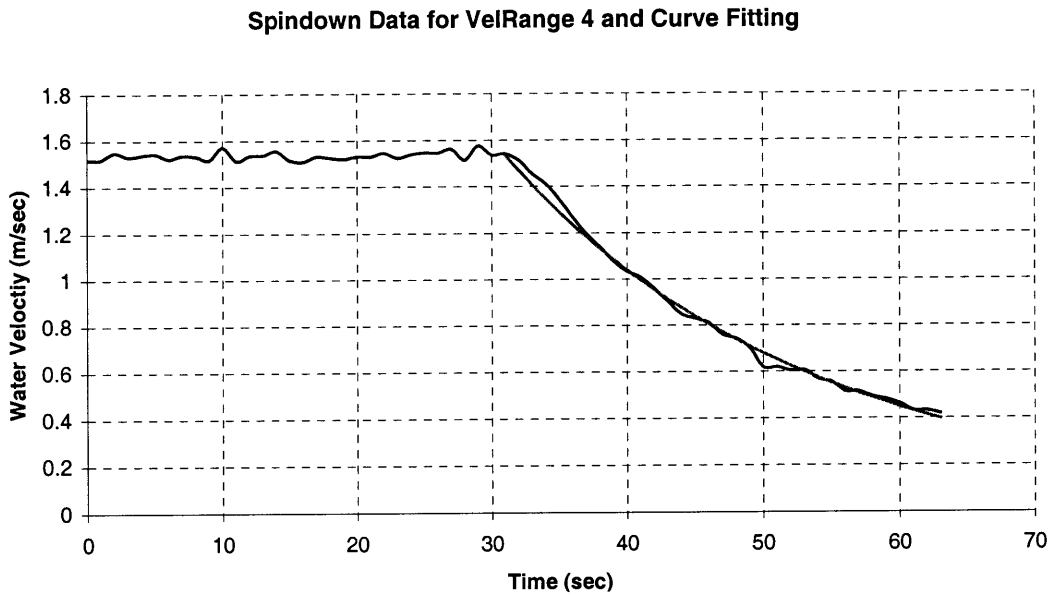

Figure 4.3: Spindown date from high water velocity recorder in velrange 4. The depth of moving water is 12 cm and the height of water surface is 25 cm above tank bottom. The curve fitting provides:

$$V_w(t) = \frac{1.533}{(1+0.002114*t)^{20.636}}$$

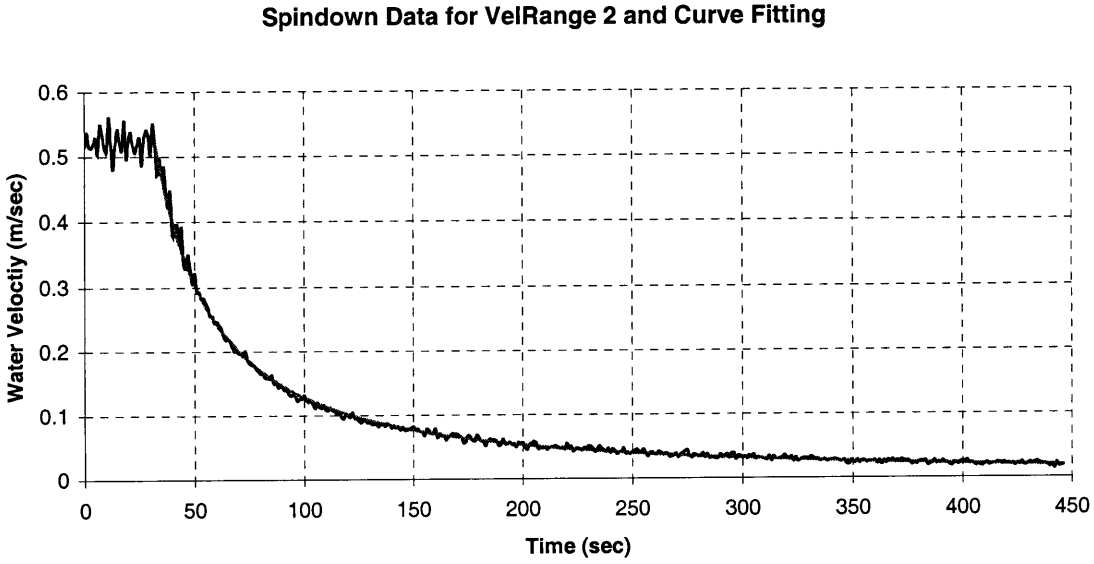

Figure 4.4: Spindown date from low water velocity recorder in velrange 2 for the same experiment as in Figure 4.3.

The curve fitting provides:

$$V_w(t) = \frac{0.5222}{(1+0.0028562*t)^{1.3014}}$$

4.5 Derivative of the water velocity

Once a curve fitting formula that has unique values of n and k is obtained for each spindown experiment, shear stress is calculated, see equation (3.16). The general form of the curve fitting model is:

$$V_w(t) = \frac{V_m}{(1+k\cdot t)^n} \tag{4.13}$$

Differentiation with respect to time, gives:

$$\frac{\partial V_w}{\partial t} = \frac{-nkV_m}{(1+k\cdot t)^{n+1}} = \frac{-nkV_w}{(1+k\cdot t)} = -nkV_w\left(\frac{V_m}{V_w}\right)^{\frac{1}{n}} \tag{4.14}$$

In the last expression, time t does not appear explicitly. This expression is used to calculate the shear stress.

4.6 Paddle RPM and air speed

In all the experiments, air speed was measured by an anemometer at a fixed location in the tank as shown in Figure 1.2. At high RPM, the generated spray wets the anemometer which cannot function properly in wet conditions. The highest RPM for which air speed was measured directly was approximately 400. For an RPM higher than 400, the air speed is found by extrapolation, or alternatively, we can abandon the use of air speed and instead use the RPM with a certain length that represents the effective paddle radius. This radius multiplied by the rotational velocity provides a measure for the air speed at the anemometer height.

Using a curve fitting for Figure 4.5, the effective paddle radius for the curve fitting is:

$$R_{ef} = 0.0369\frac{60}{2\pi} = 0.352 \quad m \tag{4.15}$$

This value is reasonable for an effective paddle radius at the point where the anemometer is placed. Its value is not sensitive to the water levels above the false

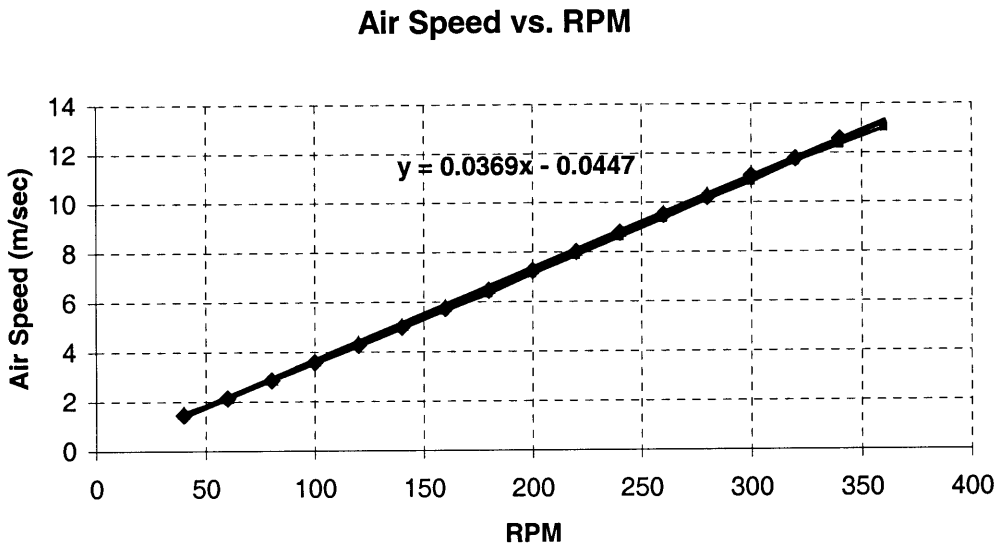

Figure 4.5: Air speed vs. RPM for three experiments with false bottom. The water surface in all experiments is 25 cm above tank bottom. The water levels above the false bottom are 8, 12 and 16 cm. The air speed is practically the same for the three experiments.

bottom. To cross check, the air speed has been measured for various water levels as shown in the Figure 4.6. Therefore, the air speed for all ranges of RPM can be calculated using $R_{ef} = 0.352 \quad m$:

$$V_a = \frac{RPM}{60} 2\pi \, R_e = 0.03686 \cdot RPM \quad m/\sec \tag{4.16}$$

In section 5 we calculate the drag coefficient using U_{10}, the extrapolated wind velocity at a 10 meter height above the water surface. Alternatively we use a V_{rpm} given by V_a in equation (4.16) to non-dimensionalize the surface shear stress by dividing it by:

$$\rho_a V_a^2 = 1.2(0.03686 \cdot RPM)^2 = 1.6305 \cdot 10^{-3}(RPM)^2 \tag{4.17}$$

The density of air is assumed to be at $T_a = 20\ K$ as $\rho_a \cong 1.2 \frac{kg}{m^3}$

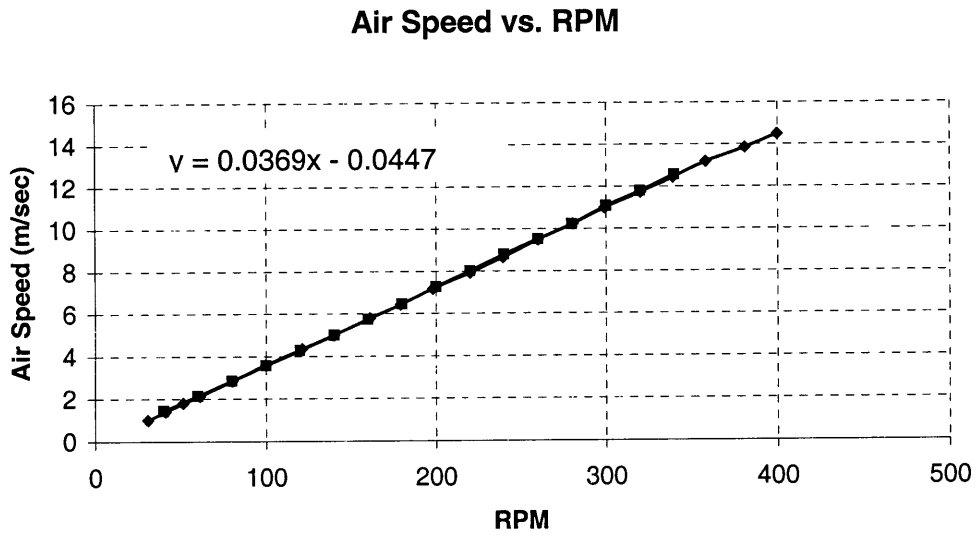

Figure 4.6: Air speed vs. RPM for two experiments. The water surface in one is 25 cm above tank bottom and the second is 12 cm above tank bottom. The air speed vs. RPM is the same for the two experiments.

The air speed did not seem to be sensive to the placement of the anemometer in the radial direction. However, an induced Ekman flow of the air was detected since the maximum air velocity near the outer wall was not in the horizontal direction but slightly downward as illustrated in Figure 4.7.

4.7 Ekman flow of the water and air

When the wind wave tank is empty and the paddle generates airflow, it has been observed that small water drops on the tank bottom tends to spiral toward the tank center. In the bulk of the rotating air there is an equilibrium between the pressure gradient in the radial direction and centrifugal forces. However, near the tank bottom the air velocity is reduced due to shear stresses within the boundary layer, leading to a reduction in the centrifugal forces. Therefore, the radial pressure gradient is greater

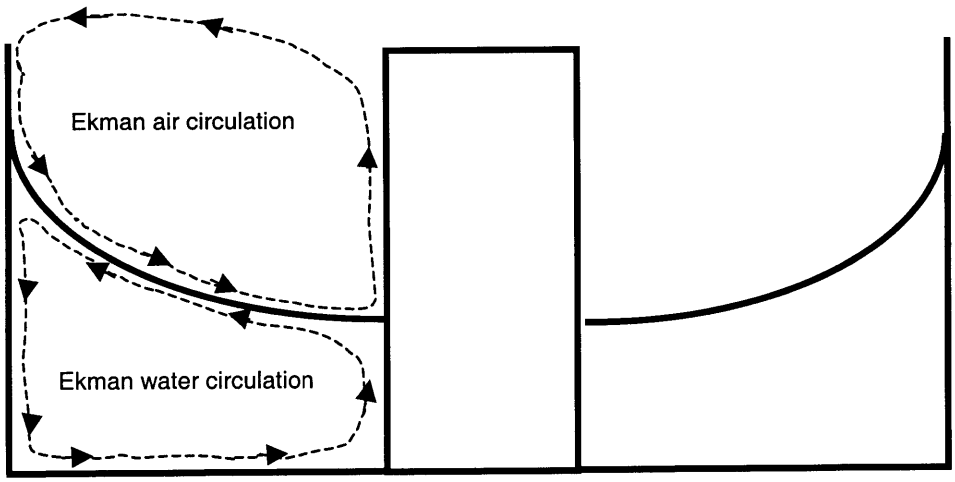

Figure 4.7: Ekman circulation of water and air in the radial direction.

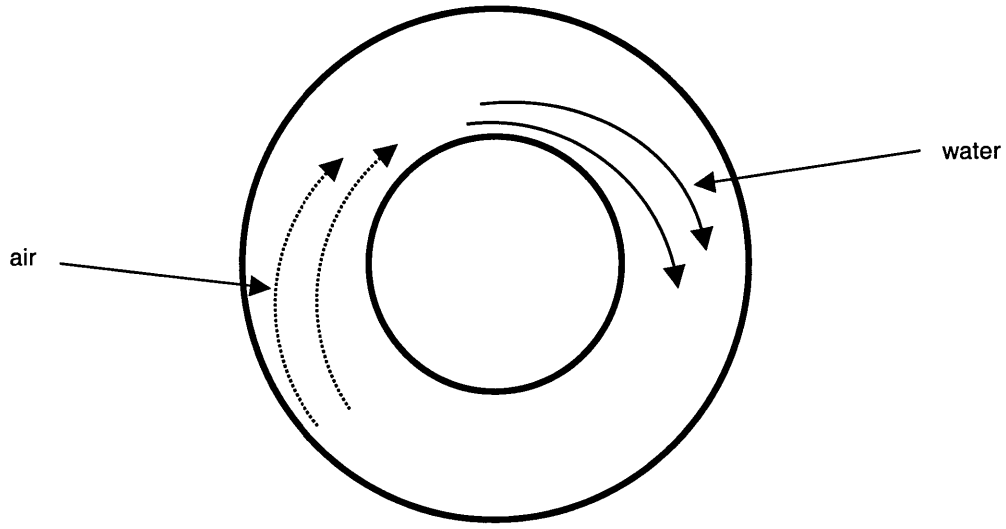

Figure 4.8: Upper view of the spiral flows of water and air near the water surface.

than the centrifugal force resulting in inward motion of the water drops near the tank bottom.

The same mechanism works when the tank is filled with rotating water. Near the tank bottom there is, in addition to the tangential velocity, a velocity component in the radial direction toward the tank center. The water is upwelling near the inner wall and on the

water surface the water motion spirals outward as shown in Figure 4.8. As for the air motion, it spirals inward near the water surface as shown in Figure 4.8. Near the inner wall, air is upwelling and it is possible that this upwelling air assists the upwelling of the water spray.

It is entirely possible that for some wind conditions, inertial oscillations of the radial water flow become unstable. Although the radial water velocity is expected to be much smaller than the tangential velocity, the radial velocity occupies a larger cross section area than the cross section area for tangential velocity. Therefore, it is possible that these oscillations, in addition to waves, cause substantial perturbations in the measured tangential water velocity.

4.8 Aerodynamics of water spray in the wind wave tank

Experiments at high RPM are intended to simulate hurricane conditions. At a paddle angular velocity of 300-400 RPM, water spray begins to form in the tank. At this RPM range, the air velocity at a height of 0.2 meter above the water surface is about 10 m/sec. The thickness and the height of the spray increase with RPM. At about 700 RPM the spray reaches the paddle height.

Unfortunately, the dynamics of ocean spray is very different from the dynamics of water spray in the wind wave tank. The semi-quantitative analysis and discussion below provide an introduction for the aerodynamics of the water spray in the tank and illustrates the limitations of the apparatus.

Observations in the wind wave tank show that the water drops have an outward spiral trajectory. The water drops are thrown by the centrifugal force onto the outer wall, forming a film that is drained back to the water surface. The equations of motion in cylindrical coordinates for a drop that is ejected from the water surface are:

z:
$$m\frac{\partial V_z}{dt} = -mg - C_{DZ}(V_z)\rho_a V_z^2 \pi d^2$$

θ:
$$m\frac{\partial V_\theta}{\partial t} = C_{D\theta}(V_{\theta\,rel})\rho_a V_{rel}^2 \pi\, d^2$$

r:

$$m\frac{\partial V_r}{\partial t} = m\frac{V_\theta^2}{r} - C_{DR}(V_r)\rho_a V_r^2 \pi\, d^2$$

and

$$V_{\theta\, rel} = V_{\theta\, air} - V_\theta$$

Where m and d are the drop mass and diameter, respectively, $C_{DZ}(V_z)$ is the drag coefficient for the vertical motion of the drop in the z direction and is dependent on the instantaneous Reynolds number. Similar expressions are defined for the drag coefficients for the drop motion in the θ and r directions. V_θ is the drop velocity in the tangential direction, $V_{\theta\, rel}$ is the relative velocity between the tangential air and drop velocities. V_r is the drop velocity in the radial direction. Here $V_z = V_z(r, z, t)$, $V_\theta = V_\theta(r, z, t)$ and $V_r = V_r(r, z, t)$. Also, due to the boundary layer over the water surface, $V_{\theta\, air} = V_{\theta\, air}(r, z)$. The initial condition of this system of nonlinear differential equations is the ejection velocity of the drop from the water surface, $V_{zo}(t = 0, z = 0, r)$

A complete solution of these equations is not relevant to our studies and is beyond the scope of this work. A qualitative evaluation of the fate of large and small drops is the following:

For a small drop (a few microns) the drag force is large in comparison to inertia. An ascending drop from the surface will accelerate by drag rapidly to the wind tangential speed, which is on the order of 10 m/sec. The tank radius is $R_{av} \cong 0.4\, m$ so the radial acceleration $\frac{V_\theta^2}{R_{av}} \cong \frac{10^2}{0.4} \cong 250\, \frac{m}{\mathbf{sec}^2}$. Clearly, such a drop accelerates and hits the outer wall instead of falling back to the water surface. Only those drops which are ejected with small upward velocity and do not reach a substantial height, will fall back to the surface. It is observed that these drops will create a film on the outer wall and drain back to the water surface.

For a large drop (a few hundred microns) the inertia force is large in comparison to the drag. These drops are expected to reach greater height in the tank due to its initial upward velocity but the drops will accelerate slowly by the tangential velocity of the wind. For a drop larger than a certain critical size, gravity is larger than radial acceleration and the drop falls back to the water surface. Visual inspection of the wind wave tank during operation shows that water drops are ejected upward near the inner wall, perhaps due to the ascending Ekman airflow and the inner wall is clear of water film.

5. A procedure for experiments and analysis

5.1 Introduction

The experimental work on the wind wave tank included the tank construction, instrument setup and debugging, design and the execution of the experiments. In order to provide calibration and enable future researchers to use the apparatus without unnecessary delay, this section outlines, step by step, the procedure for the drag experiments and their analysis.

5.2 Measuring the water and air velocities

The steady-state water velocity is measured vs. paddle RPM. The lowest RPM is 40 and the highest is about 800, depending on the amount of water in the tank. The RPM is changed by increments of 20. The ADV should be set up in advance for various water velocity ranges as outlined in section 4.4.

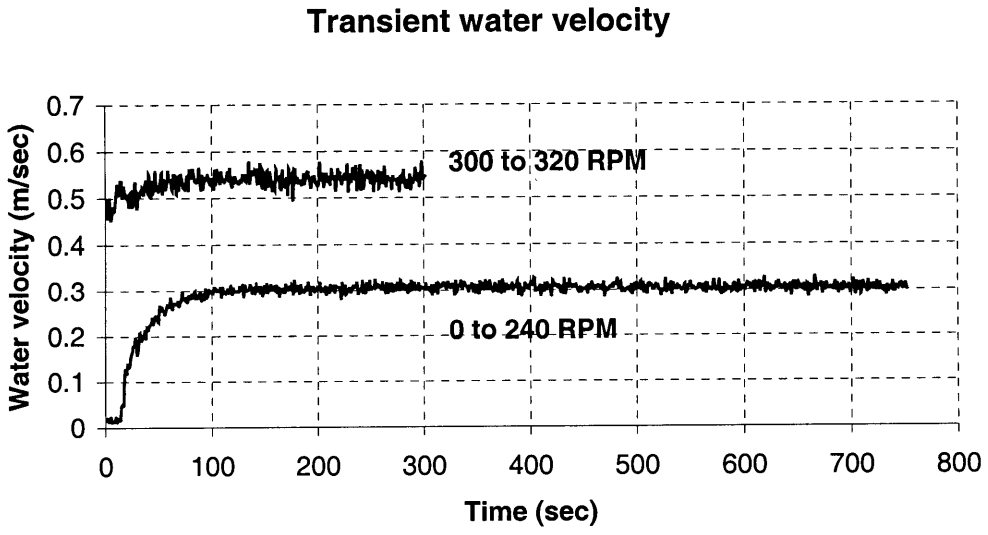

Figure 5.1: Timesries of water velocity for RPM changes. The time necessary to bring the water to steady-state velocity is approximately 100 seconds (for 12 cm water depth above false bottom which is placed 13 cm above tank bottom).

At low RPM, the time necessary to bring the water to steady state is long and it is generally shorter for high RPM. For an intermediate 200-400 RPM, the necessary time is about 2 minutes. For the lowest 40 RPM the time is long and could reach 7-10 minutes.

Once the water velocity reaches steady-state, a recording of the water velocity is done for 30-60 seconds and is averaged for each RPM. The anemometer also measures the air speed. The air speed vs. RPM relationship is outlined in section 4.6. The relative air velocity between the air and water is calculated by subtracting the water velocity from the air velocity.

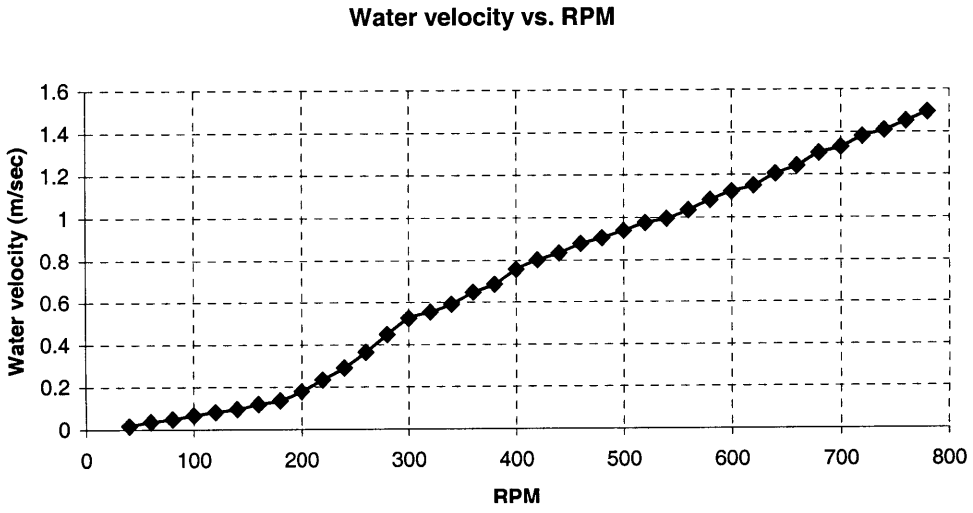

Figure 5.2: Typical water velocity vs. RPM. Around 200-300 RPM the surface becomes rough, causing a marked increase in the slope of velocity vs. RPM (for 12 cm water depth above false bottom placed 13 cm above tank bottom).

5.3 Spindown, curve fitting and the time derivative of water velocity

The spindown and curve fitting procedures are described in section 4.4. To repeat, the spindown and the curve fitting are performed in order to calculate the n and k of the water velocity vs. time given by the general expression:

$$V_w(t) = \frac{V_m}{(1 + k \cdot t)^n} \tag{4.13}$$

Where V_m is the water velocity at the start of the spindown, $t = 0$. Once the curve fitting is performed (by Solver command of Excel) the best values of n and k are found as shown in Figures 4.3 and 4.4. Their values are used to calculate the time derivative of the velocity:

$$\frac{\partial V_w}{\partial t} = -nkV_w \left(\frac{V_m}{V_w} \right)^{\frac{1}{n}} \tag{4.14}$$

The derivative is used in equation (3.32) to calculate the shear stress over the parabolic water surface:

$$\tau_{pf} = \frac{-1{,}050 \cdot H \cdot \frac{\partial V_w}{\partial t}}{PF_{torque}} \tag{3.32}$$

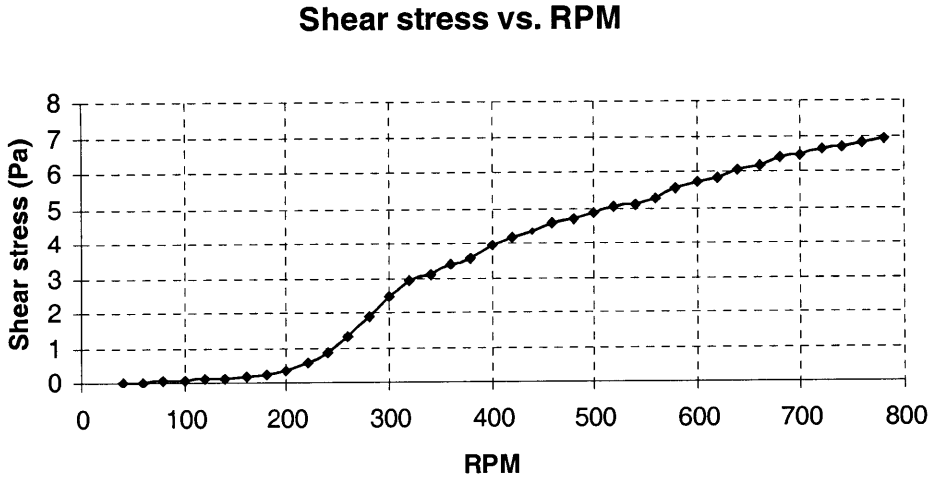

Figure 5.3: Typical shear stress vs. RPM. Around 200-300 RPM the surface becomes rough, causing a marked increase in the slope of the stress (for 12 cm water depth above false bottom which is placed 13 cm above tank bottom).

Where the subscript pf stands for parabolic factor, H is the depth of the rotating water and PF_{torque} is the parabolic torque factor given by equation (3.31):

$$PF_{torque} = 0.0006\,V_w^6 - 0.0209\,V_w^5 + 0.0903\,V_w^4 - 0.0459\,V_w^3 + 0.0184V_w^2 - 0.0027\,V_w + 1.0001 \tag{3.31}$$

The friction velocity is obtained using:

$$u_* = \sqrt{\frac{\tau_{pf}}{\rho_a}} \tag{5.1}$$

Where ρ_a is the air density, estimated as $1.2\ Kg\ m^{-3}$

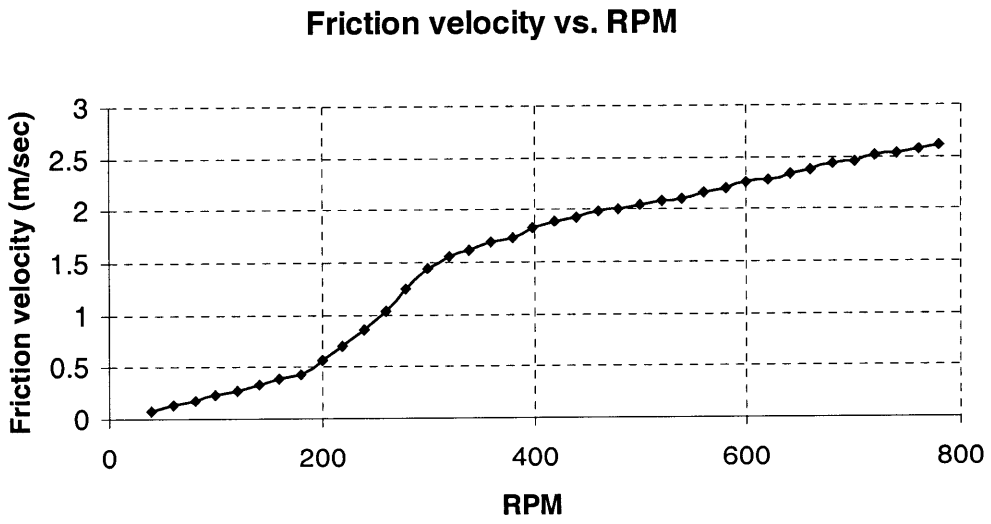

Figure 5.4: Typical friction velocity vs. RPM (for 12 cm water depth above false bottom which is placed 13 cm above tank bottom).

5.4 Drag coefficient vs. "RPM velocity"

There are two approaches for the calculation of the drag coefficient. The first is non-dimensionalizing the shear stress by dividing it by the dynamic pressure of the wind

speed at the height of the anemometer. The expression for dynamic pressure as a function of RPM is derived in section 4.6:

$$\rho_a V_{RPM}^2 = 1.2(0.03686 \cdot RPM)^2 = 1.6305 \cdot 10^{-3}(RPM)^2 \tag{4.17}$$

Therefore, the drag coefficient is:

$$C_D = \frac{\tau_{pf}}{\rho_a V_{RPM}^2} = \frac{\tau_{pf}}{1.6305 \cdot 10^{-3}(RPM)^2} \tag{5.2}$$

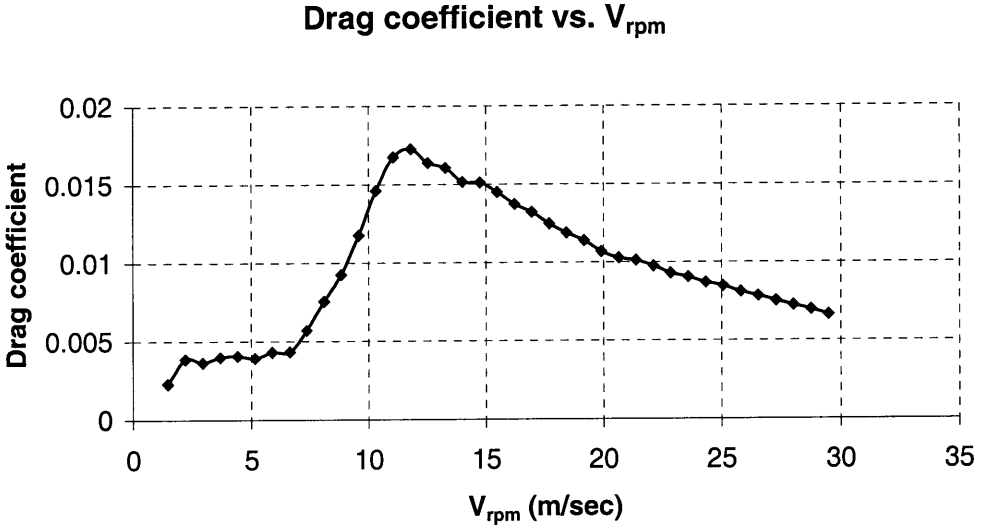

Figure 5.5: Typical drag coefficient vs. "RPM air velocity" (for 12 cm water depth above false bottom which is placed 13 cm above tank bottom).

However, the drag coefficient vs. V_{rpm} can be used only for comparison between different experiments that have the same distance between the paddle and the water surface.

5.5 Drag coefficient vs. U_{10}

The drag coefficient vs. U_{10} is calculated using the assumption that the wind velocity has a logarithmic profile and the wind speed at 10 m height is found by extrapolation. An

intermediate step is the calculation of the "roughness" of the water surface. The expression for this is:

$$\frac{u_a}{u_*} = \frac{1}{k}\ln\left(\frac{z_a}{z_0}\right) \tag{5.3}$$

Where u_a is the relative air velocity over the water surface, measured at height z_a, and $k = 0.41$ is the Von Karman coefficient. The anemometer is placed at $0.425\,m$ above the tank bottom. When the water surface height measured from the bottom of the tank is H, the expression for z_a is:

$$z_a = 0.425 - H \tag{5.4}$$

If the experiment involves a false bottom placed at height H_{fb} above the tank bottom and the depth of the water above the false bottom is H then:

$$z_a = 0.425 - H - H_{fb} \tag{5.5}$$

Equation (5.3) enables the calculation of the roughness z_0:

$$z_0 = z_a \cdot \exp\left(-k\frac{u_a}{u_*}\right) \tag{5.6}$$

The air velocity at a height of 10 m above the water surface is found by re-arranging equation (5.3):

$$U_{10} = \frac{u_*}{k}\ln\left(\frac{10}{z_0}\right) \tag{5.7}$$

The non-dimensional drag coefficient is obtained by dividing the shear stress by the

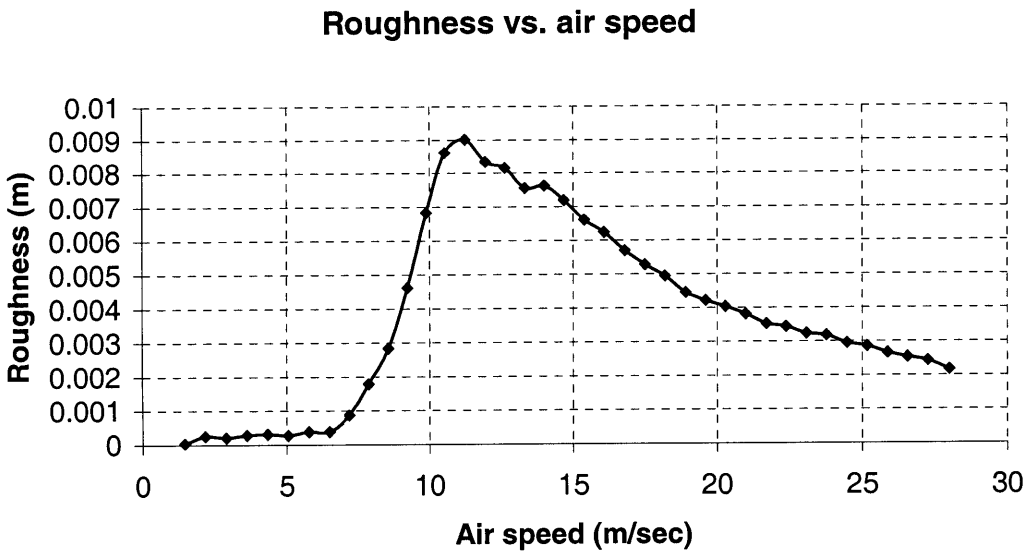

Figure 5.6: Roughness in meter vs. the relative air speed u_a over the water surface in the tank. The calculated roughness length ranges is 1-10 mm. These values do not represent the amplitude of the waves over the water surface.

dynamic pressure at the reference air velocity U_{10} obtained in equation (5.7). The drag coefficient is:

$$C_D = \frac{\tau_s}{\rho_a U_{10}^2} = \left(\frac{u_*}{U_{10}}\right)^2 \tag{5.8}$$

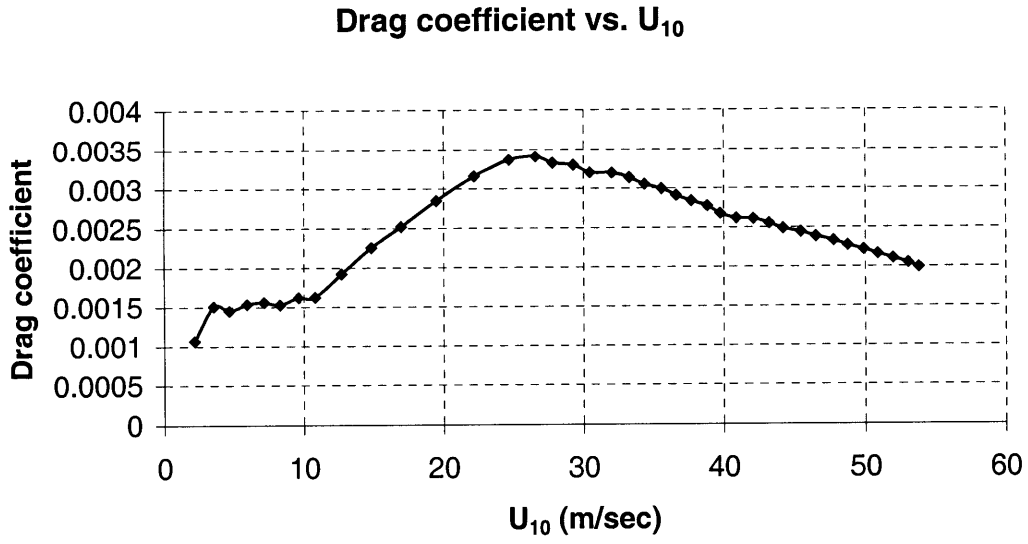

Figure 5.7: Drag coefficient vs. the wind speed at a height of 10 meter above the water surface.

6. Experimental results, discussion and conclusions

6.1 Introduction

The scientific goal of this study is to determine the dependence of the drag coefficient on wind speed. Before examining these results, a comparison between characteristics of a few experiments is shown. Such comparison is important for identifying the limitations of the apparatus and help in suggesting future modifications and experiments.

6.2 The limited tank height

The false bottom is a valuable component of the facility. It can vary the distance from paddle to the water surface with out changing the amount of water in the tank. Unfortunately, the possible height changes implemented by the false bottom are no more than 20 cm due to the height of the tank.

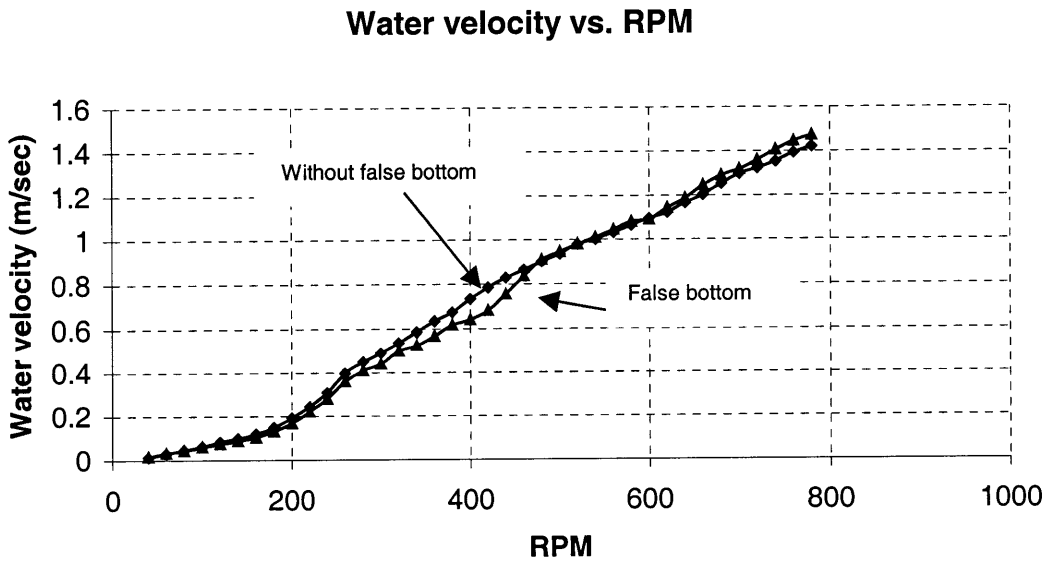

Figure 6.1: Water velocity vs. RPM for 14 cm water depth with and without false bottom. The false bottom is placed 11 cm above the tank bottom.

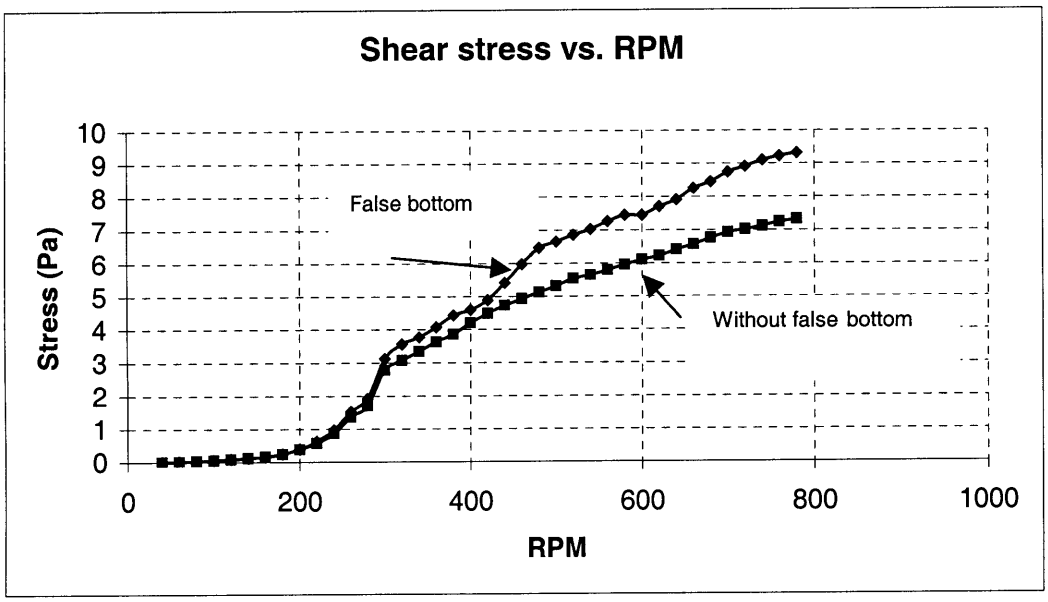

Figure 6.2: Shear stress vs. RPM for 14 cm water depth with and without false bottom. The false bottom is placed 11 cm above the tank bottom.

Figures 6.1 and 6.2 demonstrate this point. The water velocities for two experiments, one with false bottom and one without are the same. There are some discrepancies for the shear stress at high RPM and these can be attributed to the spray that reaches the paddle faster for the elevated water surface.

In further studies it might be useful to consider modifying the wind wave tank by increasing its height to about 3-5 meters. In such a tank, the false bottom position could be changed by meters, not centimeters. Also a tall tank where the paddle is much higher than the water surface will prevent the water spray from reaching the paddle blades.

To complete the comparison between the two cases with and without false bottom (shown in Figures 6.1 and 6.2), Figure 6.3 shows the drag coefficient vs. U_{10}. Figure 6.4 compares the drag coefficient vs. U_{10} for 12 cm water depth with and without a false bottom. In all the four cases the drag coefficient peaks at approximately $U_{10} = 25\, m/\mathbf{sec}$ and its maximum value is 0.0035-0.0040.

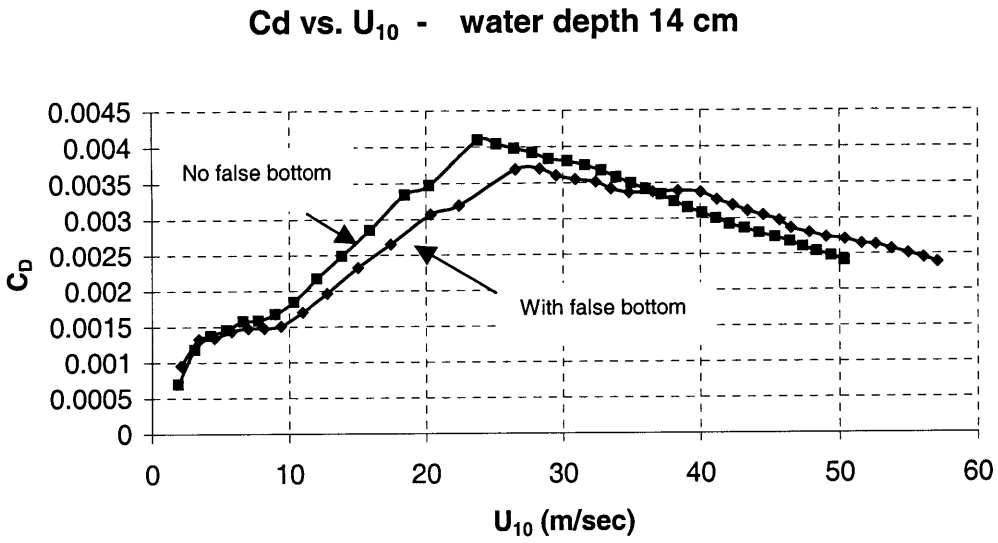

Figure 6.3: Drag coefficient vs. U_{10} for 14 cm water depth with and without false bottom. The false bottom is placed 11 cm above the tank bottom.

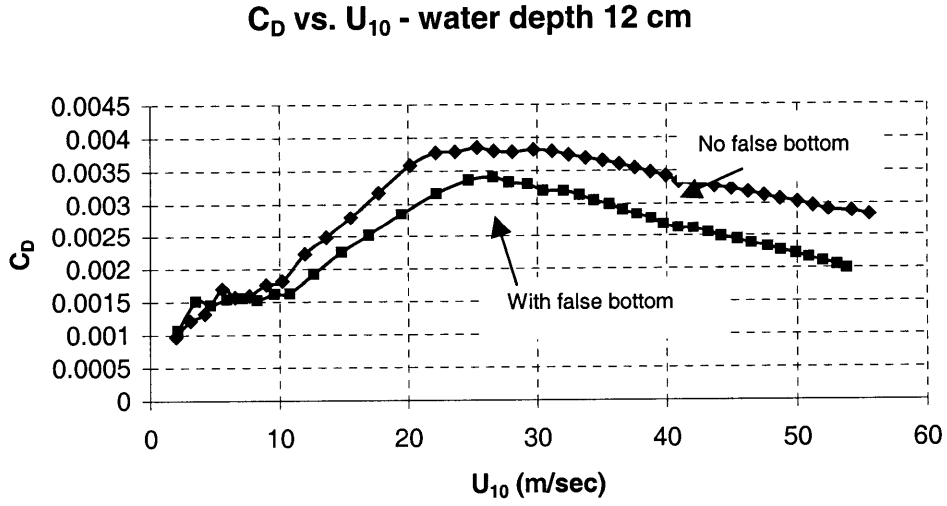

Figure 6.4: Drag coefficient vs. U_{10} for 12 cm water depth with and without false bottom. The false bottom is placed 13 cm above the tank bottom.

6.3 Apparatus and instrument failures

The results shown in section 6.2 are provided for two extreme positions of the false bottom. The highest water surface level with the false bottom was 25 cm. Without the false bottom the surface height is simply the water depth. The maximum difference in water levels for the experiments was only 13 cm.

Numerous experiments were performed for water depth of 8, 10, 12, 14 and 16 cm using various elevations of the false bottom. As outlined in section 5, comparing $C_D \; vs. \; V_{RPM}$ is meaningful only for experiments where the water surface level is the same and where the water depth varies.

The lowest water depth was 8 cm. It has been found that for this depth, the ADV cannot measure the water velocity in the middle of the water column. The velocity measurement by the ADV is done 5 cm above the ADV's fingers. Since the lowest position of the ADV's fingers is 2 cm above the false or real bottom, the velocity measurement is done 7 cm above the bottom. For 8 cm water depth, therefore, the velocity was measured 1 cm below the surface. Due to the waves, the ADV measures the velocity at a point where bubbles were generated or, periodically, at a point that was not immersed in water. Therefore, the 8 cm water depth experiments are not useful.

On the other hand, experiments that used 16 cm water depth could not reach high wind speed. The reason is that the maximum power of the electric motor is not enough to propel a large amount of water at high RPM. Therefore, at high RPM the 16 cm water depth experiment was interrupted repeatedly due to fuse burning. Future modification of the tank should include a larger and more powerful electric motor.

Useful experiments are those where the water depth was 10, 12 and 14 cm. However, it is important to note that for the 10 and 12 cm water depth, the ADV did not measure the water velocity in the middle of the water column since the lowest measurement point is 7 cm above the tank or false bottom.

At high RPM the water velocity reached 1.5 - 1.7 m/sec. Due to the parabolic shape of the water surface, the distance from the water surface to the paddle near the outer wall

is different from the distance near the inner wall. According to Figure 3.4, this difference can reach 15 cm for $V_w \cong 1.7\ m/\sec$. This introduces an error in calculating z_a, the distance from the water surface to the paddle, that is used in the calculation of U_{10} (see section 5.5). The highly parabolic water surface for high RPM also alters the moment of inertia of the water mass, and this also introduces an error in the calculation of the shear stress.

It was planned that the power of the electric motor would be measured for various experiments. However, the digital display of the instantaneous power kept oscillated, preventing a reliable reading. First Electric Motor Service, Inc is now addressing this problem.

6.4 Drag coefficient vs. U_{10}

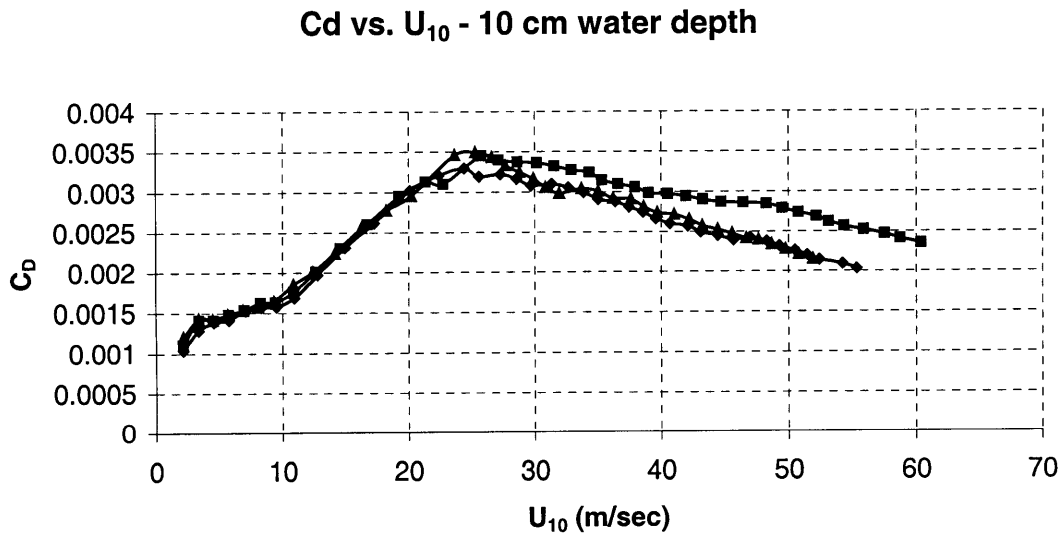

Figure 6.5: Drag coefficient vs. U_{10} for 10 cm water depth. Height of false bottom:

■ 13 cm, ▲ 11 cm, ◆ 15 cm.

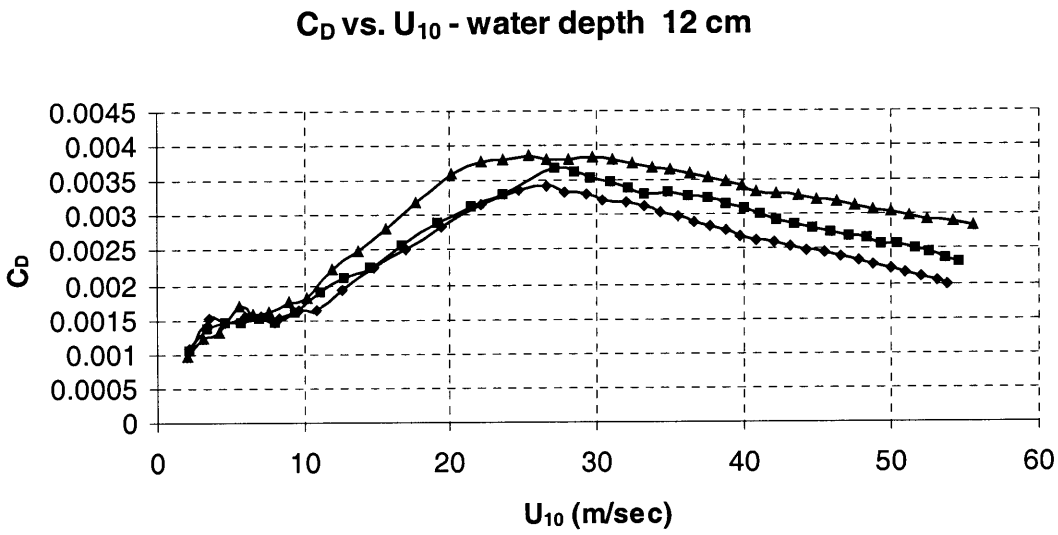

Figure 6.6: Drag coefficient vs. U_{10} for 12 cm water depth. Height of false bottom:

■ 11 cm, ▲ 0 cm, ◆ 13 cm.

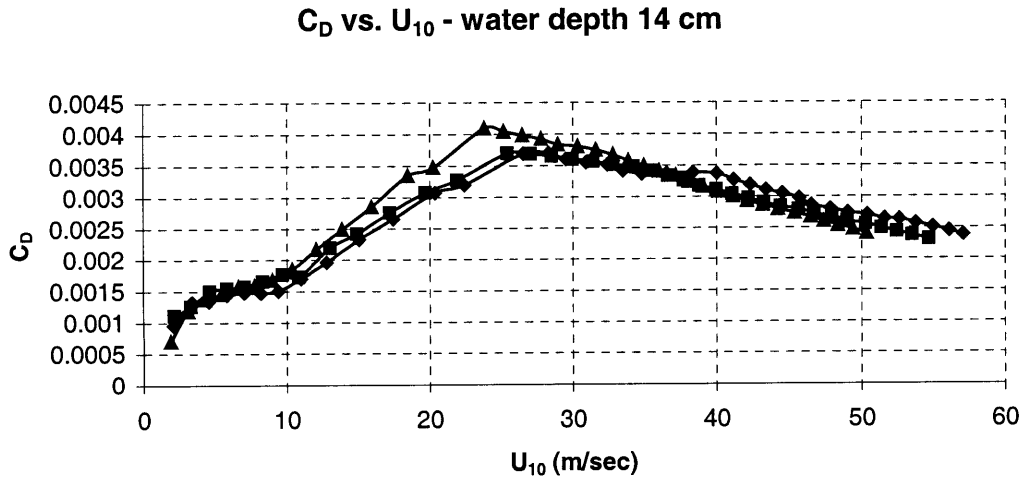

Figure 6.7: Drag coefficient vs. U_{10} for 14 cm water depth. Height of false bottom:

■ 9 cm, ▲ 0 cm, ◆ 11 cm.

Figures 6.5, 6.6 and 6.7 show a consistent pattern. The maximum C_D is 0.3-0.4 and occurs at $U_{10} \cong 25 \frac{m}{\mathbf{sec}}$. Above this velocity, the drag coefficient gradually decreases which indicates that it acts as a positive feedback for hurricane wind speed. Below the critical U_{10}, there is a sharp increase of C_D with increasing velocity. This pattern is consistent. For low wind speed, C_D is somewhat similar to that of Liu et al (1979), but his model shows a continuous increase of C_D beyond the critical U_{10}.

The role of the water spray in the rotating system might be important in determining the drag coefficient for high RPM or high U_{10}. One possible error for C_D at high RPM is introduced by the spindown from high RPM. In this procedure, as soon as the power is cutoff, water spray over the water surface ceases to exist even if the water speed is still high. Therefore, water spray does not affect the shear stress during the spindown, although it may play an important role during the steady state operation at high RPM.

6.5 Recommendations

This pilot experiments have been crucial in developing the wind wave tank for a complete experimental investigation of the momentum and enthalpy transfers in high wind speed over the ocean. The study concentrated on the fluid mechanics of the rotating water in the tank. Experiments were performed using only fresh water. No seawater, monolayer, or surfactants were applied.

It seems that there are two major issues that should be addressed in further investigation of the drag. The first may involve the reconstruction of the tank, increasing the distance between the paddle and the water surface to a few meters, as outlined in section 6.3. A bigger electric motor will enable operating the tank with larger amount of water.

The second issue is further investigation into the role of water spray in the tank and its effect on the drag. This investigation will also help to better understand the role of water spray in the evaporation experiments.

Addressing these issues will help in the next step that includes the investigation of enthalpy transfer or evaporation from the water surface in the tank in high wind speed. The drag experiments proved to be cumbersome and time consuming. It is anticipated that the evaporation experiments will be even more demanding.

Thesis References:

Alamaro, M., 1999: "On the Feasibility of Generating and Storing Winter Ice to Meet Water Demands in the Summer," Mechanical Engineer's Degree Thesis, Massachusetts Institute of Technology, May, 1999.

Andreas, E.L., et al., 1995: The spray contribution to net evaporation from the sea: A review of recent progress. *Boundary-Layer Meteorology* 72: 3-52.

Andreas, E.L., & Emanuel, K.A., 1999: Effects of sea spray on tropical cyclone intensity. *Preprints of the 23rd Conf. Hurricanes and Tropical Meteor., Amer. Meteor. Soc.*, Boston.

Andreas, E.L., and Decosmo, J. 1999: Sea spray production and influence on air-sea heat and moisture fluxes over the open ocean: in Air-Sea Exchange: Chapter 13 in *Physics, Chemistry and dynamics*, Kluwer Academic Publishers.

Barnes, G.T. and La Mer, V.K., 1962: The Laboratory Investigation and Evaluation of Monolayers for Retarding the Evaporation of Water, in *Retardation of evaporation by monolayers*: *Transport Processes*, Academic Press, New York, 35.

Barnes, G.T., 1986: Adv. Colloid Interface Sic.; *J. Hydro.* **145**, 165.

Barnes, G.T., 1997: *Colloids Surfaces*, **A 126**, 149.

Bistre, M. and Emanuel, K.A., 1998: Dissipative heating and hurricane intensity. *Meteoric. Atoms.* Physic. 65, 233-240

Black, P.G.; Holland, G.J.; and Purdon, V. :Observations of sea-air temperature difference in tropical cyclones as a function of wind speed: importance of spray evaporation. In: J.D. Jasper and P.J. Meighen (ends) *Parametrisation of Physical Processes: Papers Presented at the Fifth BMRC Modeling Workshop,* November, 1993. BMRC Research Report No. 46, Melbourne: Bureau of Meteorology Research Centre (1994) p. 87.

Drummond, C.J.; Elliot, P.; Furlong, D.N.; Barnes, G.T., 1992: *J. Colloid Interface Sci.*, **151**, 189.

Emanuel, K.A., 1986: An air-sea interaction theory for tropical cyclones. Part I. *J. Atmos. Sci.*, **42**, 1062-1071.

Emanuel, K.A., 1988: The maximum intensity of hurricanes. *J. Atmos. Sci.*, **45**, 1143-1155.

Emanuel, K. A., 1991: The theory of hurricanes. *Annual Review of Fluid Mechanics*, 23: 179-96.

Emanuel, K. A., 1995a: Sensitivity of tropical cyclones to surface exchange coefficients and a revised steady-state model incorporating eye dynamics. *J. Atmos. Sci.*, 52, 3969-3976.

Emanuel, K. A., 1995b: The behavior of a simple hurricane model using a convective scheme based on subcloud-layer entropy equilibrium. *J. Atmos. Sci.*, **52**, 3959-3968.

Emanuel, K. A., 1997: Some aspects of hurricane inner-core dynamics and energetics. *J. Atmos. Sci.*, **54**, 1015-1026.

Emanuel, K. A.: Andreas, E.L., Private communications.

Fairall, C.W.; Kepert, J.D., and Holland, G.J., 1994: The effect of sea spray on surface energy transports over the ocean. *The Global Atmosphere and Ocean System* **2,** 121-142.

Fox, R.W, and McDonald, A.T. 1998: *Introduction to Fluid Mechanics*. John Wiley & Sons, Inc., New York.

Fukuda, K; Kato, T.; Machida, S.; Shimizu, Y.J., 1979: *Colloid Interface Sci.*, **68**, 82.

Incropera, F.P. ;DeWitt, D.P., : *Fundamentals of Heat and Mass Transfer*. John Wiley & Sons, New York.

Landsea, C.W., and Peilke, Jr., R.A., 1998: Nornalized hurricane damages in the United States: 1925-95. *Wea. and Frcst.*, **13**, 621-631.

Lighthill, J., 1998: Fluid mechanics of tropical cyclones. *Theoretical and computational Fluid Dynamics,* 10: 3-21.

Liu, W.T.,Katsaros, K.B. and Businger J.A., 1979: Bulk parameterization of the air-sea exchange of heat and water vapor including the molecular constraints at the interface. *J. Atmos. Sci.* 36, 1722-1735.

Lundquist, J., 1999: Surface drag and momentum exchange in hurricane conditions. Summer Research Paper, WHOI.

McNamee, C.E.; Barnes, G.T.; Gentle, I.R.; Peng, J.B.; Steitz, R.; Robert, R.J., 1998: *Colliod Interface Sci.,* **207**, 258.

Rouault, M.P.; Mestayer, P.G.; and Schiestel, R., A., 1991: model of evaporating spray droplet dispersion. *J. Geophys. Res.* **96**, 7181-7200.

Rosenthal, S.L., 1971: The response of tropical cyclone model to variations in boundary layer parameters, initial conditions, lateral boundary conditions, and domain size. Mon. Wea. Rev., 99, 767-777.